UCLA
UCLA Previously Published Works

Title

CO Oxidation Mechanisms on CoO x -Pt Thin Films

Permalink

https://escholarship.org/uc/item/2rc5n39n

Journal

Journal of the American Chemical Society, 142(18)

ISSN

0002-7863

Authors

Kersell, Heath
Hooshmand, Zahra
Yan, George
et al.

Publication Date

2020-05-06

DOI

10.1021/jacs.0c01139

Peer reviewed

CO oxidation mechanisms on CoOx-Pt thin films

Heath Kersell[1], Zahra Hooshmand[2], George Yan[7], Duy Le[2], Huy Nguyen[7], Baran Eren[1], Cheng Hao Wu[1], Iradwikanari Waluyo[3], Adrian Hunt[3], Slavomír Nemšák[4], Gabor Somorjai[1,5], Talat S. Rahman[2], Philippe Sautet[7,8], Miquel Salmeron[1,6]

[1]Chemical Sciences Division, Lawrence Berkeley National Laboratory, Berkeley, CA, 94720, United States

[2]Department of Physics, University of Central Florida, Orlando, Florida 32816, United States

[3]National Synchrotron Light Source II, Brookhaven National Laboratory, Upton, New York, 11973, United States

[4]Advanced Light Source, Lawrence Berkeley National Laboratory, Berkeley, California, 94720, United States

[5]Department of Chemistry, University of California, Berkeley, California, 94720, United States

[6]Department of Materials Science and Engineering, University of California, Berkeley, California, 94720, United States

[7] Department of Chemical and Biomolecular Engineering, University of California, Los Angeles, United States

[8] Department of Chemistry and Biochemistry, University of California, Los Angeles, United States

ABSTRACT: The reaction of CO and O_2 with submonolayer and multilayer CoO_x films on Pt(111), to produce CO_2, was investigated at room temperature in the mTorr pressure regime. Using operan do ambient pressure X-ray photoelectron spectroscopy and high pressure scanning tunneling microscopy, as well as density functional theory calculations, we found that the presence of oxygen vacancies in partially oxidized CoO_x films significantly enhances the activity of CO oxidation to form CO_2 upon exposure to mTorr pressures of CO at room temperature. In contrast, CoO films without O-vacancies are much less active for CO_2 formation at RT, and CO only adsorbed in the form of carbonate species stable up to 260° C. On submonolayer CoO_x islands, the carbonates form preferentially at island edges, deactivating the edge sites for CO_2 formation, even while the reaction proceeds inside the islands. These results provide a detailed understanding of CO oxidation pathways on systems where noble metals such as Pt interact with reducible oxides.
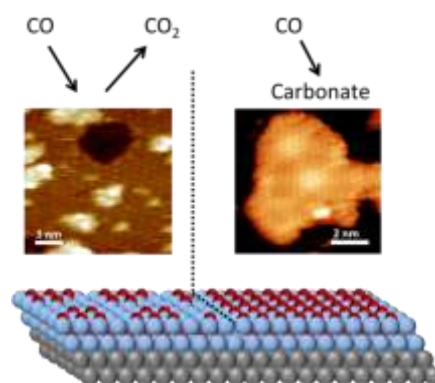
1. Introduction

The reaction of carbon monoxide with oxygen to form CO_2 ($CO + O_2 \rightarrow CO_2$) is crucial for exhaust gas processing in automobiles and stationary CO sources, and is widely studied as a prototype reaction for understanding fundamental catalytic phenomena. As a result, the search for low temperature catalysts for this reaction remains an active area of research. [1-4] Platinum catalysts are widely used to oxidize CO to CO_2, but the cost of Pt group metals has driven efforts to replace these materials with more earth-abundant alternatives. Certain transition metal oxides, e.g. CoO_x (1<x<1.33) and CuO, also exhibit low temperature activity for CO_2 formation. Cobalt oxides in particular are active at ambient temperatures. [5] Nevertheless CoO_x catalysts can suffer from deactivation under reaction conditions, [6,7] a process attributed to water dissociation to form hydroxyls, which react with CO to form bicarbonates that are stable across a broad temperature regime. [8-12]

CO oxidation to form CO_2 or carbonates on CoO_x catalysts can proceed via multiple reaction pathways depending on the sample temperature, O_2:CO ratio, phase and structure of the catalyst, and nature of the adsorbed species. [13,14] Recent reports indicate that Pt nanoparticles supported on cobalt oxide (CoO_x) exhibit unexpectedly high CO_2 formation activity relative to pure Pt, much greater than that of Pt nanoparticles on other metal oxides.[15] In the further development of these catalysts it is important to understand the mechanisms underlying their activity. To that end we report the results of operando investigations into the surface structure and composition of CoO_x–Pt catalysts under mild reaction conditions of room temperature (RT) and pressures in the mTorr regime. We use a model system where the oxide is deposited on the noble metal substrate. [16,17] These inverse systems consist of atomically thin CoO_x films grown on Pt(111), which facilitates the investigation of their atomic and chemical structure using high pressure scanning tunneling microscopy (HPSTM) and ambient pressure X-ray photoelectron spectroscopy (APXPS). The objective is to understand the role of the structure and oxidation state of CoO_x under CO oxidation conditions, and to determine the processes occurring at the noble metal-oxide boundary. Density functional theory calculations (DFT) were also performed to elucidate detailed reaction steps.

2. Methods

1   HPSTM and APXPS measurements were performed in separate ultrahigh vacuum (UHV) systems with initial base pressures
2   of 3×10^{-10} Torr and 5×10^{-9} Torr, respectively. The main residual gases in the latter were water and hydrogen, along with smaller
3   partial pressures of CO and CO_2. The Pt(111) surface was cleaned by cycles of Ar^+ ion sputtering (1.5 keV, 15 minutes) and
4   annealing (700° C, 5 minutes), followed by annealing in 5×10^{-8} Torr of O_2, then a final flash anneal to 800° C. Sample cleanliness
5   was checked with Auger electron spectroscopy or XPS.

6   Cobalt films were grown by evaporation of Co in vacuum from a 99.99+% pure Co rod (Goodfellow) using a commercial e-
7   beam evaporator. The films were then oxidized by exposure to O_2 at RT or 60° C, as noted in the following. Deposition rates
8   were calibrated with a quartz crystal microbalance. To ensure CO purity, a carbonyl trap was used during experiments with CO
9   gas. The HPSTM measurements were performed in a home-built STM with a commercial RHK controller. Pt-Ir tips were used in
10   all STM experiments.

11   The APXPS measurements were performed at beamline 23-ID-2 (IOS) of NSLS-II at Brookhaven National Laboratory. Unless
12   otherwise noted, photon energies of 1000 eV, 730 eV, and 485 eV were used to generate photoelectrons with approximately 200
13   eV kinetic energy for the Co 2p, O 1s, and C 1s spectra, respectively. Binding energies (BE) are referenced to the Fermi edge for
14   each spectrum. Information regarding the fitting procedures used for XPS analysis is provided in the supplemental information
15   (section S1). Additional measurements to test the reversibility of certain reaction steps were performed at beamline 11.0.2 of the
16   Advanced Light Source of Lawrence Berkeley National Laboratory (section S4).

17   Submonolayer CoO_x films with coverage of 0.3–0.5 ML were prepared to study the effect Pt has on activity when exposed
18   alongside the CoO_x films. Multilayer films were prepared to determine the activity of the CoO_x with no Pt exposed. Except where
19   indicated, the multilayer films had CoO_x coverages between 1.8 and 2.2 ML and will be referred to in the following as 2 ML films.
20   The films contained mixtures of Co^{2+} (CoO) and Co^o (metallic Co), with their ratio depending on O_2 exposure and sample
21   temperature.

22   Two separate sets of DFT calculations were performed using the Vienna ab-Initio Simulation Package (VASP)[18], and
23   projector-augmented wave[19,20] and plane wave basis set methods. In both cases, the Perdew-Burke-Ernzerhof functional[21] was
24   used. One set of calculations employed spin-polarized DFT (SP-DFT). For that approach, a (10×6×5) slab of Pt(111) was structured
25   from its optimized interplane lattice parameter of 3.92 Å. The submonolayer of CoO had dimensions of 5×6 unit cells with Co
26   atoms on FCC sites of the underlying Pt(111) substrate. The other approach included a Hubbard-like repulsion term due to the
27   strong self-interaction of the Co 3d electrons. These DFT+U calculations accounted for the presence of gas phase reactants by
28   considering the entropic contributions of reactant and product species to the Gibbs free energy, and were also used to study the
29   behavior of partially oxidized CoO_x films, as observed experimentally. Additional calculation details are provided in Section S6.

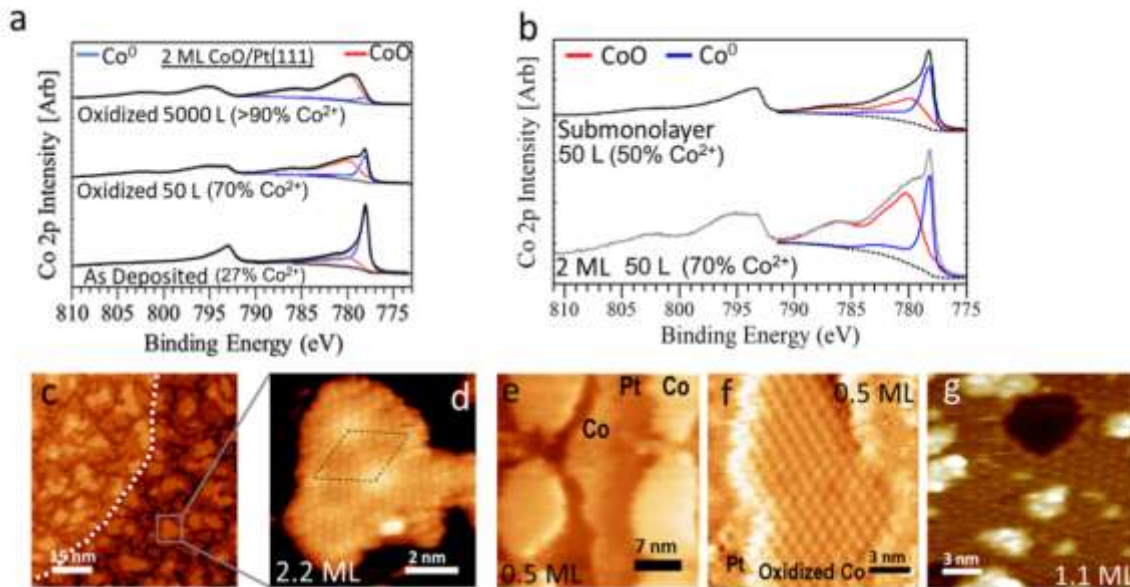
Fig. 1. a) XPS, in the Co 2p region, of a 2 ML Co film on Pt(111). *Bottom spectrum*: as deposited film. *Middle spectrum*: after exposure to 50 L O_2, *Top Spectrum*: after exposure to 5000 L O_2. Spectra are deconvoluted into Co^o (blue) and Co^{2+} (red) components. The Shirley background (shown in black) is subtracted to calculate the component areas. The average oxide content is 27%, 70%, and >90%, respectively. The top spectrum contains predominantly Co^{2+}, but a second component is present which could be either Co^o or Co^{3+}.; b) *Top*: Co 2p region of a 0.5 ML film after exposure to 50 L O_2 at RT (resulting in 50% CoO). *Bottom*: The middle spectrum from (a) is repeated here for comparison (2 ML film, 50 L O_2 exposure); c) STM image of an oxidized 2 ML film, consisting of a full first layer with islands of 2nd and 3rd layer. In the image, the film covers two terraces of the Pt substrate, separated by a step (marked by the dashed line). This surface was oxidized by exposure to 50 L O_2 at 60° C; d) Image of a 3rd layer island from (c), with a hexagonal 3.4 Å periodic structure and a contrast modulation period of 2.6 nm (dashed lozenge); e) STM image of a 0.4 ML Co film before O_2 exposure, showing exposed Pt and Co^o islands; f) after 50 L O_2 exposure submonolayer Co islands become partially oxidized, forming a structure with 1 nm periodicity; g) image of a nearly complete monolayer showing the same 1 nm periodicity, with small 2nd layer islands (brighter areas) and exposed Pt (dark spot).

30

3. Experimental Results

To understand the role and synergy of Pt and CoO in CO oxidation, we studied each of the following steps: (a) oxidation of the Co films on Pt by O_2 exposure; (b) reaction of pure CO gas with the CoO_x films; and c) reactions with mixtures of CO and O_2.

3a. Oxidation and structure of CoO_x films

CoO_x films were produced by exposing Co films, deposited on Pt(111), to O_2 gas. The extent of conversion of metallic Co (Co^o) into CoO (Co^{2+}) was controlled by the magnitude of the O_2 exposure. Figure 1a shows XPS in the Co 2p region for 2 ML CoO_x after various O_2(g) exposures. The sample was held at 60° C during O_2 exposure. Fits of the spectra with Co^{2+} and Co^o components are shown by the red and blue traces, respectively. The CoO is identified by its characteristic broad structure with a satellite peak above 785 eV, and metallic Co by the sharp peak at 778.2 eV.[22] It is also possible to form oxides containing Co^{3+} at higher temperatures and pressures. The Co 2p spectra of Co^o, Co^{2+}, and Co^{3+} are distinguished by the BE of their peaks, distinct satellite structures, and spin-orbit splitting.[22,23,24] Upon initial O_2 gas exposure, all films studied here showed only Co 2p signatures characteristic of Co^o and Co^{2+}. Afterwards however, carbonate and carbide also form as the films are exposed to CO, which we show in the following sections. Further details of the Co 2p fittings are provided in the supporting information.

The as-deposited Co films always contained some amount of oxide (Fig. 1a, bottom spectrum), likely from oxidation by water in the background gas.[25] Exposure to 5000 L of O_2 converted the films almost completely into CoO (>90% Co^{2+}) (top spectrum), while intermediate exposures produced mixtures of Co^{2+} and Co^o (middle spectrum).

The extent of oxidation in the films depends not only on the O_2 exposure, but also on the film thickness. In the 2 ML films, many Co atoms were located beneath the top layer. Hence, the subsurface layers oxidized less completely than the top one. Counterintuitively however, submonolayer films oxidized less than the 2 ML films when given the same O_2 exposure, in spite of all Co atoms in submonolayer films being exposed to the O_2 gas (Figs. 1b, S1).* Ultrathin Sn films on Pd(111) were also previously reported to exhibit a resistance to oxidation as compared with thicker films.[26]

STM images of the surfaces of 2 ML, 1 ML, and submonolayer oxide films are shown in Fig. 1c-g. The 2 ML film whose image is shown in Fig. 1c contains ~70% Co^{2+} according to XPS (Fig. 1a, middle spectrum). Its first layer covers the Pt substrate, with partial 2nd and 3rd layers on top. In the image, the film spans two Pt terraces separated by a step, its edge marked by a dotted line. Magnified images of the 3rd layer reveal a hexagonal lattice with 3.4 Å periodicity and a contrast modulated by a larger 2.6 nm periodicity (Fig. 1d). This is characteristic of CoO films with a Moiré pattern due to lattice mismatch between adjacent layers, similar to other authors' findings.[27-30] The lattice periodicity depends on the atomic layer, with the exposed area of the 2nd and 1st layers showing periodicities of 3.7 Å and 4 Å respectively (not shown). While 30% of the Co atoms remain metallic (Fig. 1a), only CoO structures are found at the surface, indicating that the Co^o is mostly located in subsurface layers.

The STM image in Fig. 1e shows submonolayer Co islands before O_2 exposure, and Figs. 1f and 1g show submonolayer and ~1 ML film images after O_2 exposure (Fig. 1b, top spectrum). Both CoO_x images show ordered structures with 1 nm periodicity, which is $2\sqrt{3}$ times the underlying Pt(111) periodicity. This structure produces the top XPS spectrum shown in Fig. 1b (with ~50% Co^{2+}). The apparent height of the partially oxidized monolayer is 1.7 Å, similar to that reported for single bilayers of CoO.[31]

We emphasize that CoO_x films with 1 ML coverage or less were oxidized to a lesser extent than multilayer films, even with the same preparation conditions.

3b. CO adsorption and reaction with CoO_x films

Before studying the reaction of CoO_x films with CO, we determined the nature and amount of contaminant species accumulated during the film preparation. Fig. 2a and 2b show XPS of the C 1s region from a 2 ML CoO_x film comprised of >90% CoO (Fig. 1a, top spectrum). Four spectral features are visible in the XPS after forming the oxide (Fig. 2a,b curve (1)): a peak at 284 eV, which we attribute to hydrocarbon species (CH_x) with a coverage estimated at less than 14% of a ML; a peak at 285.6 eV, due to background CO adsorbed on residual Co^o sites[25,32,33]; and a peak at 288.8 eV with a small shoulder at 287.8 eV, where the higher binding energy feature is consistent with carbonate species (CO_3) formed by CO adsorbed on CoO, and the lower BE feature can be explained by the simultaneous presence of
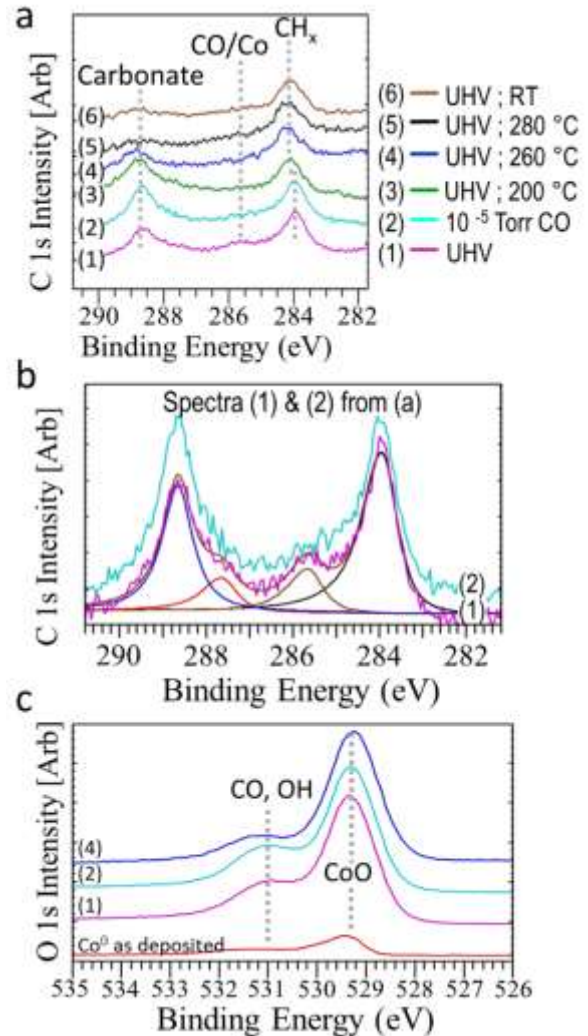
Fig. 2: XPS of the 2 ML CoO_x film from the top spectrum in Fig. 1a. a) C 1s region. Conditions are listed in the box in the top right side; b) Enlarged spectra for conditions (1) & (2). Fitting shows four components (described in the text); c) Corresponding O 1s XPS region.

bicarbonate.[34-36] These assignments are supported by the observation that heating the sample to 50° C (section S2) caused desorption of the 285.6 eV peak (CO/Co°), while the C peak at 288.8 eV persisted up to 260° C (Fig. 2a (4) & (5)). This temperature is consistent with the decomposition of carbonates formed by CO adsorbing on CoO_x.[34,37] Similar features were previously reported on Co_3O_4 (288.5 eV), TiO_2 (288.4 eV), and Cu_2O.[34-38]

The corresponding O 1s region (Fig. 2c) contains peaks at 529.3 eV from CoO, and at 531.1 eV from overlapping oxygen contributions of carbonate, OH, and CO.[25,32,34] When the sample was exposed to 10^{-5} Torr of CO, only the C 1s and O 1s peaks from the carbonate increased (blue spectra (2) in Fig. 2a,b). It is also possible that CO interacting with background water may form bicarbonate, contributing to the 531.1 eV peak. [8] The oxide peak at 529.3 eV did not change during CO exposure, indicating no reduction of the CoO_x.

Next, we studied the interaction of CO gas with a 2 ML CoO_x film containing approximately 70% CoO (30% Co°) as in Fig. 1a, middle spectrum. As mentioned above, the top layer of this film is comprised of ordered CoO structures (Fig. 1d), with Co° in the subsurface layers. Exposing this surface to CO at pressures from UHV to 140 mTorr did not change the intensity of the oxide peak at 529.3 eV in the O 1s region (Fig. 3a). This behavior is similar to that shown in Fig. 2, and indicates no reduction from the RT reaction $CO + O_{lattice} \rightarrow CO_2$. On the complete CoO top layer, CO only adsorbs to form carbonate, with peaks at 531.1 eV (O 1s) and 288.8 eV (C 1s). The intensities of these two peaks increase in parallel with CO pressure and saturate upon reaching 30 mTorr of CO, as shown in Fig. 3a and 3b, with a carbonate coverage estimated at approximately 20% of a ML. Once the carbonate coverage saturates, no further adsorption or reaction takes place unless the temperature is increased to the point where the carbonate decomposes, as shown in Fig. 2a curve (5). We note that recent work in ref. [39] reports that CO does not adsorb on CoO, whereas we observe CO adsorbing on CoO films to form carbonate. While film preparation and gas exposure conditions were different between those experiments and ours, the XPS measurements in this study provide spectroscopic evidence of CO adsorption to form carbonate.
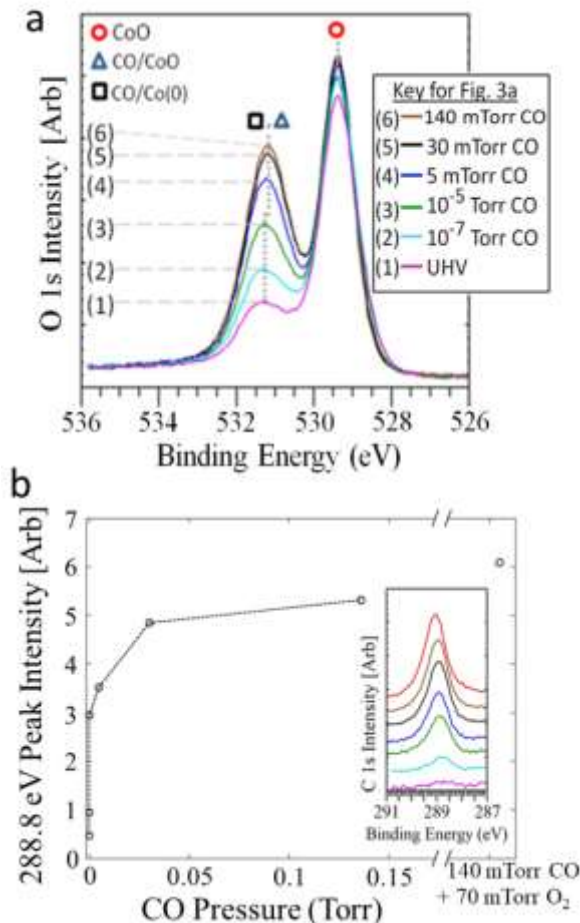
Fig. 3. a) O 1s XPS region under increasing CO pressures on a 70% oxidized 2 ML film on Pt(111). b) Intensity of the carbonate C 1s peak at 288.8 eV vs. CO pressure. Inset shows the carbonate peak for the CO pressures shown in Fig. 3a (from bottom to top) and for a CO + O_2 mixture (last point).
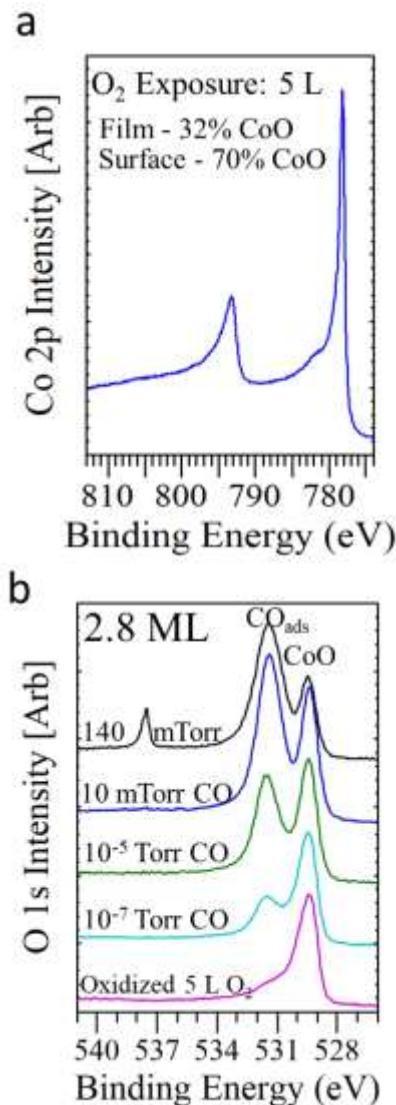

Fig. 4. a) Co 2p XPS from a 2.8 ML CoO_x film formed by exposure to 5 L O_2; total film composition ~30% CoO, surface layer composition ~70% CoO; b) O 1s region under increasing CO pressure. The intensity of the peak from CO on Co^o at 531.3 eV increases and saturates around 10 mTorr, at which point a sharp reduction in intensity of the oxide

1   The reactivity with CO is very different for oxide films where the surface is only partially oxidized, i.e., exposing some
2 metallic Co. To demonstrate this, we prepared a 2.8 ML CoO_x film by exposing a deposited Co^o film to 5 L O_2. The Co 2p
3 spectrum (Fig. 4a) of this film is dominated by a sharp metallic peak at 778.2 eV, with a small shoulder above 780 eV from the
4 oxidized component. From the relative peak areas and film thickness, we estimate that ~30% of the surface Co atoms remain
5 Co^o. The surface of this film was reduced by CO exposure at RT, as illustrated in Fig. 4b. In UHV, the O 1s region contains only
6 the peak at 529.3 eV from CoO and a small higher BE shoulder at 531.3 eV from adsorbed CO and/or OH from background gas
7 (Fig. 4b, bottom spectrum). Upon introducing CO gas in the chamber, CO adsorbs on the metallic Co (Fig. S2), and the peak
8 from CO_{ads} increases. At the same time, the reaction $CO + O_{lattice} \rightarrow CO_2$ takes place, causing a decrease in the intensity of the
9 oxide peak at 529.3 eV, clearly seen at CO pressures above 10 mTorr in Fig. 4b. CO_2 formation could also be followed by
10 measuring the CO_2 gas product using a mass spectrometer located in the second stage of the differentially pumped XPS
11 analyzer[40], as shown in Fig. 5. CO_2 is formed by reaction of CO with lattice oxygen in the films. Initially the CO_2 formation rate
12 increases with CO pressure until the lattice oxygen is depleted by the reaction. At that point, the CO_2 production decreases
13 unless O_2 is added to the CO gas, providing further oxygen for the oxidation of CO to CO_2. When O_2 is added to the CO gas in a
14 1:2 ratio, CO_2 gas formation is inhibited and CO adsorbs as carbonate on the CoO films (Figs. S2,S3), hence the reaction rate
15 remains relatively low. This mass spectrometry agrees with our results showing that partially oxidized surfaces (exposing O
16 vacancies) facilitate CO adsorption and reaction with lattice oxygen (i.e., via the Mars van Krevelen mechanism[41]) to form CO_2
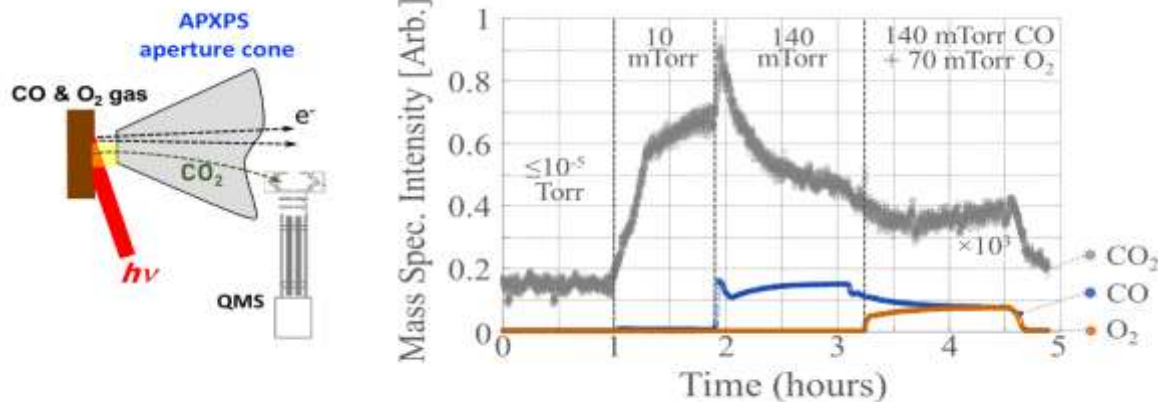17 and reduce the oxide at RT. In oxygen rich mixtures however, RT CO_2 formation is inhibited.

Fig. 5. Left: Schematic showing the mass spectrometer located in the 2nd pumping stage of the APXPS spectrometer optics. Mass spectra intensities were recorded during APXPS measurements on a 2.8 ML CoO film on Pt(111). Curves for mass 28 (CO), 44 (CO_2), and 32 (O_2) intensities are shown in blue, grey, and orange respectively. The reactant gas pressures in the sample chamber (before the aperture cone) are shown above in the graph. The curve for mass 44 (CO_2) was obtained by subtracting a background CO_2 curve (obtained using an unreactive substrate instead of the sample) from the CO_2 curve measured with the sample present.

We also note that CO_2 formation can result from CO disproportionation ($2CO \rightarrow C + CO_2$). CO dissociation can be facilitated by hydrogen adsorbed from the background gas, contributing to the accumulation of surface carbon species.[25,46] Indeed, some carbide and CH_x accumulate as the CO pressure is increased (Fig. S2), suggesting a possible second pathway for CO_2 formation. In mass spectrometry, this process is difficult to distinguish from the reaction $CO + O_{lattice} \rightarrow CO_2$, since it occurs alongside the consumption of the lattice oxygen to form CO_2. However, it is more readily understood by the O 1s and C 1s peaks of CoO_x, CH_x, and carbide in the XPS.

While other CoO_x catalysts deactivate under reaction conditions[6,7], complete deactivation was not observed during our measurements. The CO_2 formation rate decreased in pure CO as $O_{lattice}$ is consumed, but increased slightly when O_2 was added to the gas mixture. Previous investigations have shown that water readily dissociates on Co^o and CoO_x surfaces[25,32], and that the presence of water in the reactant gas can deactivate the RT reaction over time.[11] In our system, a similar role could be played by water dissociating to form OH at otherwise active sites, and then reducing the activity. In the XPS, this would produce a peak above 531 eV.[25,32] By maintaining a UHV base pressure and taking steps to maintain reactant gas purity, the background water pressure was kept low.

Decreased CO_2 formation by Co_3O_4 at higher pressures was previously correlated with reduction to CoO.[7] In agreement with this, our measurements indicate that CoO formation, at the expense of vacancy sites, strongly inhibits the reaction. Interestingly though, our results show that the CoO phase can be made active for CO_2 formation if oxygen vacancies are present. The DFT calculations presented in section 4 describe the energy landscape of the different reaction steps, with and without O vacancies. There, we show that oxygen vacancies in the CoO lattice enhance the reaction rate of CO with lattice O atoms by reducing the reaction barrier. Meanwhile, CO_2 formation suffers from much slower kinetics on surfaces without O vacancies.

3c. The Role of the CoO_x-Pt Interface

In the previous section, the CoO_x films completely covered the Pt surface. We now focus on the case where both Pt and CoO_x are exposed, i.e., samples where CoO_x islands are surrounded by bare Pt. Fig. 6a shows O 1s spectra for the 0.4 ML CoO_x film that produced the top XPS spectrum in Fig. 1b. That film is partially oxidized, containing 50% Co^o. Initially, two O peaks are
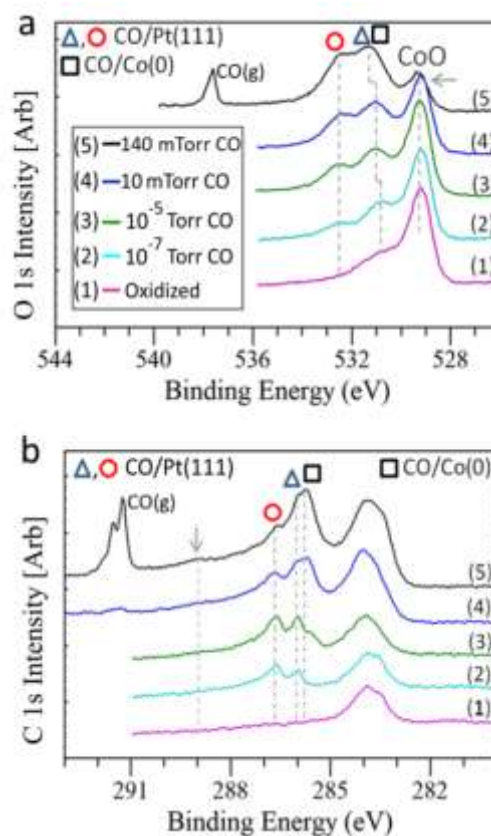

Fig. 6. XPS of a 0.4 ML CoO_x film with a 50:50 ratio of Co^o:Co^{2+}; a) O 1s region as a function of CO pressure. A sharp reduction in the oxide peak intensity occurs for CO pressures in the mTorr regime. The oxygen peaks correspond to CoO (528.6 eV), CO/Co^o (531.5 eV, square symbol), and CO/Pt bridge and top sites (531.5 and 532.5 eV, triangle and circle respectively). The C 1s region is shown in (b) for each of the conditions in (a). Gas phase peaks appear at 537.6 eV and 291.3 eV, with a vibrational satellite at 291.6 eV. (No satellite is visible in the O 1s due to lower analyzer resolution at this energy).

visible; one at 529.2 eV from CoO, and another at 530.8 eV with possible contributions from OH, CO/Co°, and CO/Pt bridge sites.[25,42] The 530.8 eV peak increases and shifts slightly to higher BE as the CO pressure increases, likely due to an increased contribution from CO/Co° (marked in Fig. 6b with a black square).[25] The O 1s peak from CO on top sites of Pt(111) is also visible at 532.5 eV (red circle).[42,43] The various CO species are better distinguished by their C 1s peaks in Fig. 6b.

The intensity of the oxide peak at 529.2 eV decreased significantly when the CO pressure reached the mTorr range. This decrease is accompanied by an increase in the intensity of the C 1s feature from CO adsorbed on Co° at 285.6 eV. In parallel with the reduction of CoO, some CO also reacts with lattice oxygen to form carbonate, producing the peak at 288.8 eV marked by an arrow.[25,32,44] At lower BE, the C 1s region contains peaks at 283.5 eV and 284 eV, which can be attributed to carbide, [25,45] and CH_x [25] accumulated during Co evaporation and by possible CO dissociation assisted by background H_2 [25,46]. These peaks gradually increase during the measurements, indicating an amount of carbidization and contamination, and potentially suggesting CO_2 formation by CO disproportionation. Peaks from the gas phase CO are visible above 10 mTorr, both in the C 1s and O 1s regions.

Addition of O_2 to the gas phase modified the extent of the two CO reactions with CoO_x (i.e. formation of carbonates, and formation of CO_2). Figure 7a plots the intensity of the C 1s peaks from CO/Co° and carbonate as a function of reactant gas pressure. Exposure to pure CO causes an initial rapid increase of the coverage of both CO/Co° and carbonate, both saturating in
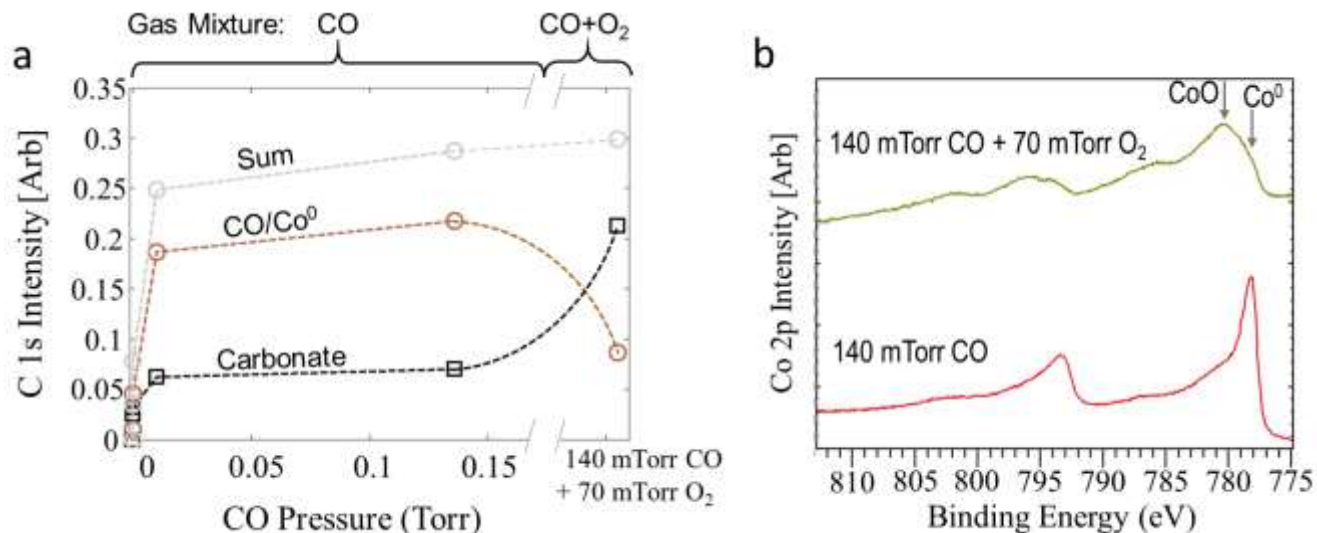

Fig. 7. a) C 1s intensities vs. pressure for carbonate at 288.8 eV (black), CO/Co° at 285.6 eV (brown), and their sum (grey). b) Co 2p XPS in 140 mTorr CO (lower), and after addition of 70 mTorr of O_2 to the gas mixture (upper).
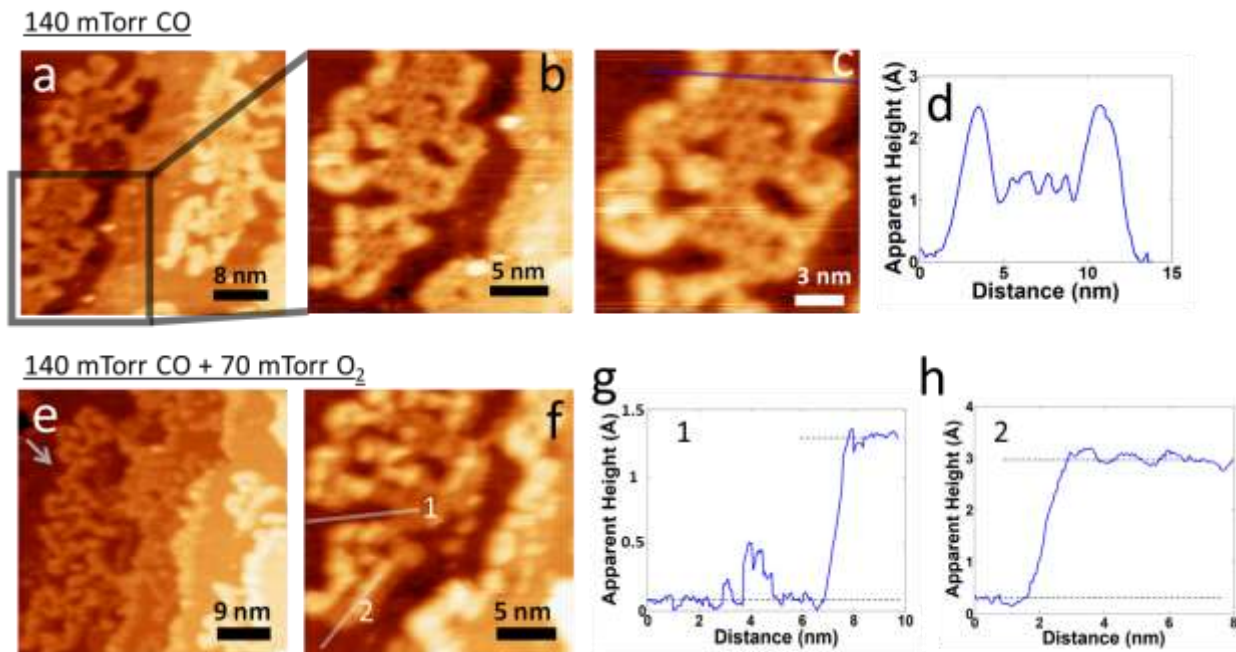

Figure 8. HPSTM images of a submonolayer CoO_x film on Pt(111) under 140 mTorr CO (a). Expanded images of the film reveal a hexagonal ordered structure at the island interiors and a high contrast edge structure (b,c). An apparent height line profile is shown in (d) along the line in (c). Images acquired under CO + O_2 mixtures are shown in (e), and (f) for the same islands in (a)-(c). Apparent height line profiles shown in (g) and (h) are along lines 1 and 2 in (f). STM Imaging Parameters: (a,b) I_t = 90 pA. V_t = 270 mV: (c) I_t = 100 pA. V_t = 300 mV: (e,f) I_t = 100 pA. V_t = 300 mV.

the mTorr pressure regime. When O_2 was added to the gas, the carbonate coverage increased and the CO/Co° decreased, with

1   the sum of the two staying nearly constant, suggesting that Co^{o} sites where CO previously adsorbed now oxidize to CoO and
2   facilitate carbonate formation. As in the case of 2 ML films, carbonate formation is observed when partially oxidized surfaces
3   transform to surfaces with few or no oxygen vacancies. This is shown in Fig. 7b where before adding O$_2$ the Co 2p spectrum was
4   sharply peaked at 778.2 eV, revealing significant metallic composition; whereas adding O$_2$ transformed the CoO$_x$ film
5   composition into mostly CoO, as indicated by the broad satellite structure in the top spectrum. We note that even after adding
6   O$_2$ to the gas mixture, about 10% of the Co remained metallic (indicated in the figure). When we pumped out the gas mixture
7   and subsequently added 140 mTorr of pure CO into the chamber, the oxide was not reduced (section S4), indicating negligible
8   activity for the RT reaction of CO with the oxide.
9   The structural evolution of submonolayer oxide films during the reaction was investigated *in situ* by HPSTM. Fig. 8a-c
10   shows images of the CoO$_x$ islands at RT (initially containing 50% Co^{2+}, as in Fig. 1b) acquired in the presence of 140 mTorr CO.
11   As shown above (Fig. 6), under these conditions the CoO$_x$ film is largely reduced and covered by CO. The film also contains a
12   small amount of carbonate, indicated by the arrow in Fig. 6b. However, XPS could not inform us about the spatial structure of
13   the system. This information is provided by HPSTM imaging. The images in Fig.8 show that under 140 mTorr CO, the island
14   edges form structures characterized by a high contrast, while the island interiors adopt an ordered hexagonal structure with a
15   periodicity characteristic of CO on metallic Co (~1 nm).[33] A line profile of the apparent height across the islands shows that the
16   edges have nearly twice the apparent height of the island interiors (Fig. 8d). These observations can be explained with the
17   hexagonal structure of the island interiors corresponding to CO adsorbed on Co^{o} and the high contrast edges to carbonate. The
18   areas covered by these interior and edge structures in the images scale approximately with the amounts of CO/Co^{o} and CO$_3$ from
19   the XPS, although convolution of the sample structure with the STM tip shape exaggerates the areas of the higher contrast
20   regions. This interpretation is further supported by the fact that adding oxygen to the gas mixture increases the amount of
21   carbonate (Fig. 7a), and increases the length and number of high contrast structures decorating the island edges. With O$_2$ in the
22   gas, this structure also appears on new edges formed at the island interiors (Fig. 8e,f). The formation of carbonate species at
23   island edges suggests that the edges do not act as reaction frontiers at RT, but are instead poisoned following the Sabatier
24   principle.
25   The formation of carbonate at the island periphery is also predicted by the DFT calculations (next section). Its easy
26   formation could be facilitated by the added influx of CO and O diffusing from the Pt to the Co island edges, and by the different
27   coordination environment there. At the island interiors on the other hand, CO and O$_2$ mostly adsorb directly from the gas
28   phase, rather than from migration across the surface. Our results imply that at RT, carbonate species form more effectively at
29   island edges, which do not act as nucleation sites for the reaction but instead are deactivated. Meanwhile reduction of the oxide
30   by the CO gas continues in the island interiors under O$_2$ lean conditions.
31   Hence, we have identified two potential roles of Pt in the oxidation of CO:
32   (i)   Exposed Pt can act as a source of reactant diffusion toward the island edges, facilitating the formation of stable carbonate
33   there, and;
34   (ii) Monolayer thick films were less easily oxidized than multilayer films (as discussed in section 3a). Ultrathin Sn films on
35   Pd(111) were also previously reported to exhibit a resistance to oxidation as compared with thicker films, where the
36   resistance was attributed to a charge transfer between the Sn and Pd.[26] Such a charge transfer could affect the CO
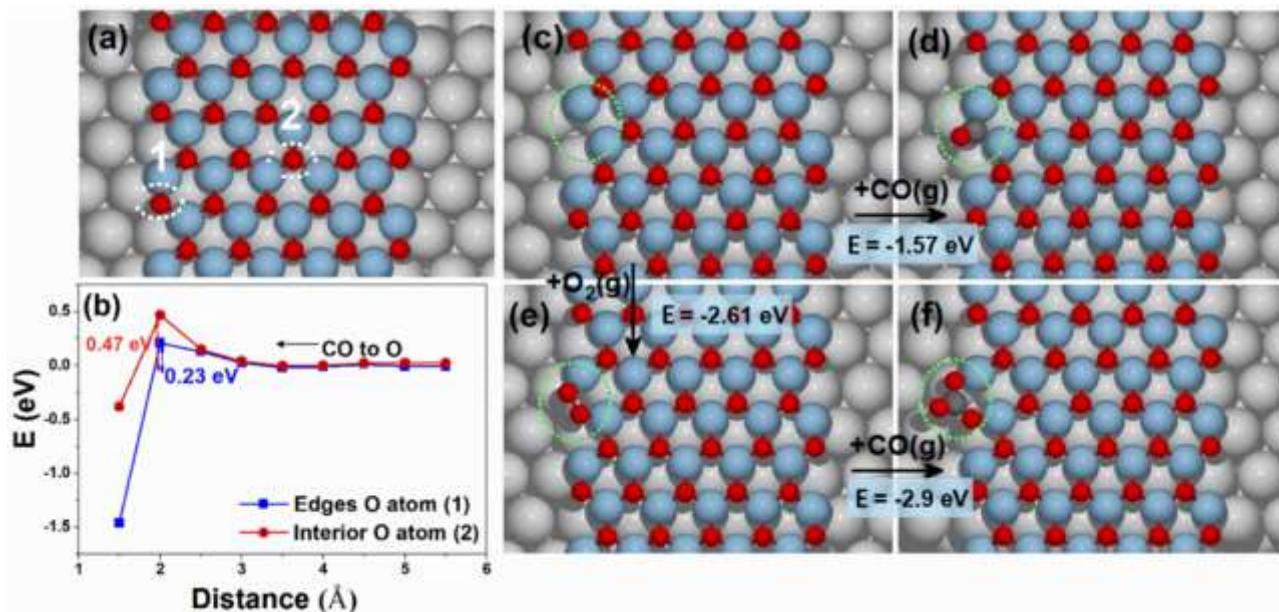

Fig. 9. a) Oxygen atoms in CoO submonolayer film at edge (1) and interior (2) sites. b) Energy vs. distance [O$_{lattice}$-CO$_{gas}$]
plot, leading to CO adsorption on lattice O at island edges (1) and interiors (2). Adsorption barriers are 0.47 eV and 0.23 eV,
respectively. c-f) O vacancy (c), where CO (d) and O$_2$ (e) can adsorb (c). O$_2$ dissociation followed by CO adsorption (e,f) leads to
formation of stable carbonate at the island edge sites. Changes in energy for each step are shown in light blue boxes. Color code
of atoms: Pt (grey), Co(blue), O(Red) and C(dark-grey).

*Energy barriers calculated using two separate approaches, employing either nudged elastic band or drag methods, described in

37   oxidation activity, potentially affecting CO$_2$ formation rates.

While the contribution of Pt to these processes requires further study, our results confirm that oxygen vacancies enhance the activity for CO oxidation to form CO_2, and that monolayer thick films exhibit unique properties potentially further influencing the activity.

4. Theoretical Interpretation

To gain a deeper understanding of the mechanisms of CO oxidation on CoO with and without oxygen vacancies, we performed density functional theory (DFT) calculations. Because of the lattice parameter mismatch between CoO and Pt(111), we performed calculations with: (a) the CoO_x under compressive strain, forced to match the bulk-terminated Pt(111) lattice; and (b) with CoO_x on an expanded Pt surface, where the Pt-Pt distance is 3.15 Å so the CoO approaches its bulk parameter. We found the energies of the various adsorption sites and reaction steps to be similar in both cases. In some calculations (Fig. 10), a Hubbard-like repulsion term (U_{eff} = 3.5 eV) was introduced. This decreases the adsorption energy of O on the CoO_x layer and renders CO_2 and carbonate formation more exothermic, but does not change the qualitative picture (Section S6b).

To investigate the role of O-vacancies found experimentally on the CoO films, two different arrangements of oxygen vacancies were studied: (I) one arrangement contained isolated atomic O vacancies; and (II) the other had 50% of CoO sites containing O vacancies, as in the structure found experimentally on mono- and submonolayer films (Fig. 1f,g).

Finally, the effect of hydroxylation of the CoO_x by background water was considered. The presence of hydroxyls at the film surface can facilitate bicarbonate formation through a barrier of 0.68 eV (Fig. S10). Bicarbonate is found to be almost as stable as carbonate, and as a result, multiple carbonate species can be present on these surfaces.

Figs. 9 and 10 show the energy and free energy landscapes for the reaction of CO with various CoO_x model surfaces. Details of the calculations are described in the Supporting Information.

The main results of the calculations can be summarized as follows:

a) On monolayer thick CoO films with no oxygen vacancies, the most favored CO adsorption site at the film interiors is atop lattice oxygen. From there, CO can oxidize to form CO_2. The resulting CO_2 can also form a bound carbonate with nearby O. Although energetically stable, this carbonate prefers to decompose and desorb as $CO_2(g)$ due to a large entropic gain. This process leaves behind an oxygen vacancy. Adsorption of CO on lattice O at CoO interior sites has an energy barrier of 0.47-0.49 eV*, and a lower barrier of 0.23 eV at island edges (Fig. 9b, 10c). However, while the activation energy for the reaction is low, the entropy of CO in the gas

Fig. 10. Relative electronic energy (ΔE) and Gibbs free energy (ΔG) profiles at RT (ΔG: blue, ΔE: red) along the reaction pathway to the formation of CO_2 and CO_3^{2-} on monolayer thick CoO_x/Pt(111) surfaces. a,b) Profiles for partially oxidized films, with 50% of sites containing O vacancies. a) ΔG and ΔE profiles for reaction directly with CO from the gas phase to form CO_2 and CO_3^{2-}. b) Profiles for the reaction of adsorbed CO/Co^o with lattice oxygen to form CO_2. c) ΔG and ΔE profiles for CO_2 and CO_3^{2-} formation on CoO with no O vacancies. The reaction occurs much faster on the partially oxidized surface in (b) ($ΔG_{TS}$ = 0.87 eV for CO*→CO_2*) than on the complete CoO surface in (c) ($ΔG_{TS}$ = 1.23 eV for $CO_{(g)}$→CO*) because the

phase raises the Gibbs free energy barrier considerably (1.23 eV at RT on the CoO island, Fig. 10c). Hence, this process has slow kinetics at RT, consistent with our observation that CoO films with few or no oxygen vacancies are not reduced by RT CO exposure during measurements over several hours.

b) When a single lattice O vacancy is present at a CoO island interior, CO molecules prefer binding to O atoms adjacent to the vacancy site, and forming CO_2, with an adsorption energy of -2.39 eV, 1.34 eV lower than at CoO sites without nearby oxygen vacancies (Table S1). This CO_2 desorbs and leaves behind further oxygen vacancies where CO can adsorb. In agreement with this observation, we also find that CO adsorbs on half oxidized layers of CoO (i.e. 50% Co^o) exothermically atop exposed Co^o. This reduces the Gibbs free energy barrier of reaction with nearby oxygen to 0.87 eV, making this surface much more active (10^6 times) than the completely oxidized surface. The resulting CO_2 desorbs, leaving behind additional oxygen vacancies. This agrees with our experimental observation that partially oxidized CoO_x surfaces are much more active for $CO_2(g)$ formation than films with few or no O vacancies.
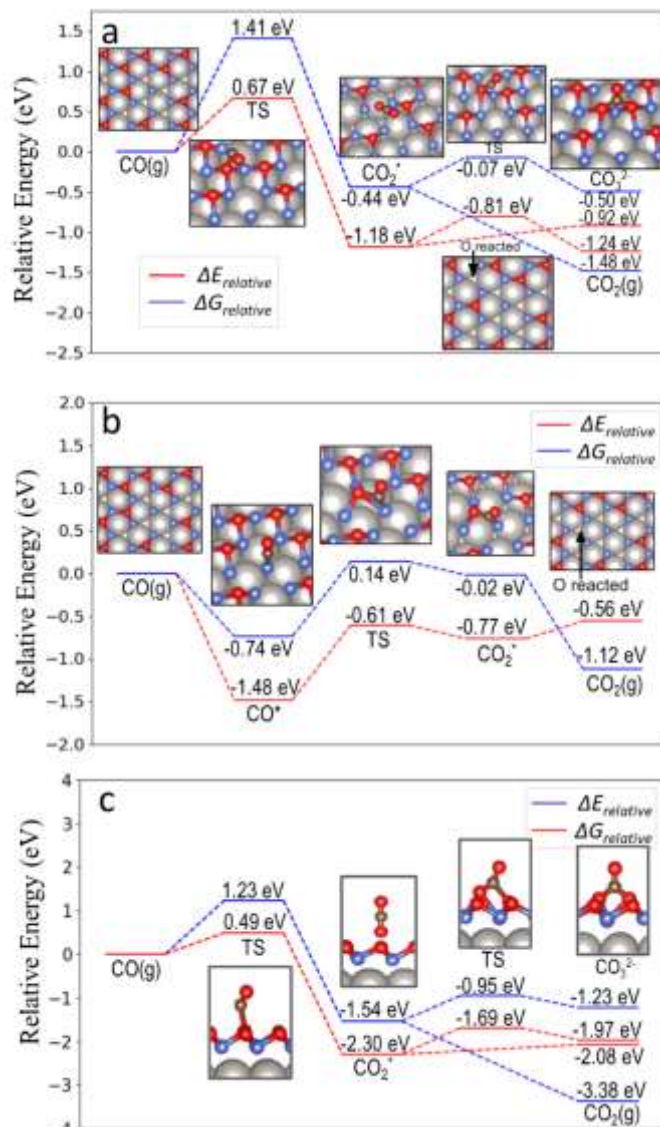
Returning to the case of isolated O vacancies in CoO islands, we also considered the case where O_2 and CO are in the gas phase together. As before, CO can react with O atoms adjacent to vacancy sites and form CO_2. This process leaves behind an O vacancy. Alternatively, O_2 can adsorb at vacancy sites, where it reacts with CO to form CO_2, and the remaining O atom replenishes lattice O at vacancy sites (Fig. S7).

c) At CoO island edges, both oxide reduction to form CO_2 and carbonate formation are possible. Which processes occurs is determined by the structure of the oxide edge sites. CO can react with O atoms at island edge sites, forming CO_2, which desorbs and leaves behind vacancies there (Fig. 9a-c). At edge O vacancies (Fig. 9c), either O_2 or CO can adsorb, lowering the energy of the system by 2.61 eV or 1.51 eV respectively. CO can react with oxygen adsorbed at these sites (Fig. 9f), forming a bridged carbonate structure with an exothermic reaction energy of 2.9 eV. Carbonate formation at CoO_x edge sites is consistent with our experimental observations, showing carbonate forming preferentially at the island edges.

Our calculations demonstrate that the presence of oxygen vacancies greatly enhances the oxidation of CO to form CO_2 on CoO films on Pt(111). Meanwhile, the reaction suffers greatly from slow kinetics at RT when no vacancies are present. These results agree with the experimental findings discussed in the previous section, and provide a detailed picture of the pathways for CO oxidation, and for the deactivation of the reaction $CO + O_{lattice} \rightarrow CO_2$ on these surfaces.

5. Conclusions

We investigated the reaction of CO and O_2 on inverse supported model catalysts consisting of atomically thin CoO_x films on Pt(111) at RT. Partially oxidized CoO film surfaces (i.e. rich in O vacancies) were found to be very active for CO_2 formation at RT. Meanwhile, CoO films whose surfaces lacked O vacancies suffered from much slower kinetics and were not reduced by RT CO exposure. These results indicate that operating with oxygen-lean mixtures of gas phase CO and O_2 is key to mitigate deactivation in low temperature conditions.

We also found that monolayer thick Co films are less readily oxidized than their multilayer counterparts. Since CO_2 formation proceeds more easily on partially oxidized films, they may provide a resistance to the slower kinetics found in films with few or no O vacancies.

When both Pt and CoO_x are exposed in submonolayer films, stable carbonate forms preferentially at the CoO island edges, making the edges inactive for RT CO_2 formation. Meanwhile, the interiors of partially oxidized surfaces are readily reduced to Co^o, where CO subsequently forms an ordered adsorbed layer. These findings suggest that complete 1 ML films with no Pt exposed, like those shown in Fig. 1g, may benefit from less carbonate formation (due to fewer edge sites) in addition to being less oxidized by exposure to O_2 than multilayer films. This scenario applies to O_2 lean conditions, and to temperatures below $260°C$, where the carbonates do not decompose. Finally, we note that the importance of O vacancies in CO_2 formation may not be restricted to CoO_x-Pt catalysts, and since surface carbonates have been reported on other transition metal oxides, these observations may also be applicable to other oxide-metal catalyst systems.

ASSOCIATED CONTENT

AUTHOR INFORMATION

Corresponding Author

* mbsalmeron@lbl.gov

Present Addresses

Heath Kersell*, Baran Eren[†]

*Advanced Light Source, Lawrence Berkeley National Laboratory, Berkeley, CA 94720

†Department of Chemical and Biological Physics, Weizmann Institute of Science, 234 Herzl Street, 76100 Rehovot, Israel

Author Contributions

The manuscript was written through contributions of all authors. All authors have given approval to the final version of the manuscript.

Notes

The authors declare no competing financial interest.

ACKNOWLEDGMENT

ADDITIONAL NOTE

The top spectrum in Figure 1b was oxidized at RT, and the bottom one was prepared at 60 °C. The holding of the submonolayer films at 60 °C during oxidation changed their extentofoxidationfrom50%Co2+to55%Co2+(FigureS1),still significantly less than that for the 2 ML films.

REFERENCES

(1) Wang, H.-. F.; R. Kavanagh, R.; Guo, Y.-. L.; Guo, Y.; Lu, G.; Hu, P. Origin of extraordinarily high catalytic activity of Co_3O_4 and its morphological chemistry for CO oxidation at low temperature. *J. Catal.*, **2012**, 296, 110-119.

(2) Vandichel, M.; Moscu, A.; Grönbeck Catalysis at the Rim: A Mechanism for Low Temperature CO Oxidation over Pt_3Sn. H. *ACS Catal.*, **2017**, 7, 7431-7441.

(3) Gatla, S.; Aubert, D.; Agostini, G.; Mathon, O.; Pascarelli, S.; Lunkenbein, T.; Willinger, M. G.; Kaper, H. Room-Temperature CO Oxidation Catalyst: Low-Temperature Metal-Support Interaction between Platinum Nanoparticles and Nanosized Ceria. *ACS Catal.*, **2016**, 6, 6151-6155.

(4) Nie, L.; Mei, D.; Xiong, H.; Peng, B.; Ren, Z.; Hernandez, X. I. P.; DeLaRiva, A.; Wang, M.; Engelhard, M. H.; Kovarik, L.; Datye, A. K.; Wang, Y. Activation of surface lattice oxygen in single-atom Pt/CeO_2 for low-temperature CO oxidation. *Science*, **2017**, 358, 1419-1423.

(5) Royer, S.; Duprez, D. Catalytic Oxidation of Carbon Monoxide over Transition Metal Oxides. *ChemCatChem*, **2011**, 3, 24-65.

(6) Jansson, J.; Palmqvist, A. E. C.; Fridell, E.; Skoglundh, M.; Österlund, L.; Thormählen, P.; Langer, V. *J.* On the Catalytic Activity of Co_3O_4 in Low-Temperature CO Oxidation. *Catal.*, **2002**, 211, 387-397.

(7) Jansson, J.; Skoglundh, M.; Fridell, E.; Thormählen, P. A mechanistic study of low temperature CO oxidation over cobalt oxide. *Top. Catal.*, **2001**, 16, 1.

(8) Weilach, C.; Spiel, C.; Föttinger, K.; Rupprechter, G. Carbonate formation on Al_2O_3 thin film model catalyst supports. *Surf. Sci.*, **2011**, 605, 1503 - 1509.

(9) Song, A.; Skibinksi, E. S.; DeBenedetti, W. J. I.; Ortoll-Bloch, A. G.; Hines, M. A. Nanoscale Solvation Leads to Spontaneous Formation of a Bicarbonate Monolayer on Rutile (110) under Ambient Conditions: Implications for CO_2 Photoreduction. *J. Phys. Chem. C*, **2016**, 120, 9326-9333.

(10) Thormählen, P.; Skoglundh, M.; Fridell, E.; Andersson, B. Low-Temperature CO Oxidation over Platinum and Cobalt Oxide Catalysts. *J. Catal.*, **1999**, 188, 300 - 310.

(11) Cunningham, D.A.H.; Kobayashi, T.; Kamijo, N.; Haruta Influence of dry operating conditions: observation of oscillations and low temperature CO oxidation over Co_3O_4 and Au/Co_3O_4 catalysts. M. *Catal Letters*, **1994**, 25, 257 - 264.

(12) Vayssilov, G. N.; Mihaylov, M.; Petkov, P. St.; Hadjiivanov, K. I.; Neyman, M. Reassignment of the Vibrational Spectra of Carbonates, Formates, and Related Surface Species on Ceria: A combined Density Functional and Infrared Spectroscopy Investigation. *J. Phys. Chem. C*, **2011**, 115, 23435-23454.

(13) Lukashuk, L.; Yigit, N.; Rameshan, R.; Kolar, E.; Teschner, D.; Hävecker, M.; Knop-Gericke, A.; Schlögl, R.; Föttinger, K.; Rupprechter, G. Operando Insights into CO Oxidation on Cobalt Oxide Catalysts by NAP-XPS, FTIR, and XRD. *ACS Catal.*, **2018**, 8, 8630-8641.

(14) Tang, Y.; Ma, L.; Dou, J.; Andolina, C. M.; Li, Y.; Ma, H.; House, S. D.; Zhang, X.; Yang, J.; Tao, F. Transition of surface phase of cobalt oxide during CO oxidation. *Phys. Chem. Chem. Phys.*, **2008**, 20, 6440-6449.

(15) An, K.; Alayoglu, S.; Musselwhite, N.; Plamthottam, S.; Melaet, G.; Lindeman, A.; Somorjai, G. A. Enhanced CO Oxidation Rates at the Interface of Mesoporous Oxides and Pt Nanoparticles. *J. Am. Chem. Soc.*, **2013**, 135, 16689-16696.

(16) Ostroverkh, A.; Johánek, V.; Kúš, P.; Romana, Š; Matolín, V., Efficient Ceria-Platinum Inverse Catalyst for Partial Oxidation of Methanol. *Langmuir*, **2006**, 32, 6297 - 6309.

(17) Rodríguez, J.; Hrbek, J., Inverse oxide/metal catalysts: A versatile approach for activity tests and mechanistic studies. *Surf. Sci.*, **2010**, 604, 241 - 244.

(18) Kresse; G., Furthmüller, J., Efficient iterative schemes for *ab initio* total-energy calculations using a plane-wave basis set. *Phys. Rev. B*, **1996**, 54, 11169-11186.

(19) Blöchl, P.E., Projector augmented-wave method. *Phys. Rev. B*, **1994**, 50, 17953–17979.

(20) Kresse, G.; Joubert, D., From ultrasoft pseudopotentials to the projector augmented-wave method. *Phys. Rev. B*, **1999**, 59, 1758–1775.

(21) Perdew, J.P.; Burke, K.; Ernzerhof, M., Generalized Gradient Approximation Made Simple. *Phys. Rev. Lett.*, **1996**, 77, 3865–3868.

(22) Biesinger, M. C.; Payne, B. P.; Grosvenor, A. P.; Lau, L. W. M.; Gerson, A. R.; Smart, R. St. C., Resolving surface chemical states in XPS analysis of first row transition metals, oxides, and hydroxides: Cr, Mn, Fe, Co and Ni. *Appl. Surf. Sci.*, **2011**, 257, 2717-2730.

(23) Ivanova, T.; Naumkin, A.; Sidorov, A; Emerenko, I.; Kiskin, M.; X-ray photoelectron spectra and electron structure of polynuclear cobalt complexes. *J. Electron Spectrosc.*, **2007**, 156-158, 200-203.

(24) Frost, D. C.; McDowell, C. A.; Woolsey, I. S.; X-ray photoelectron spectra of cobalt compounds. *Mol. Phys.*, **1974**, 27, 1473-1489.

(25) Wu, C. H.; Eren, B.; Bluhm, H.; Salmeron, M. B., Ambient-Pressure X-ray Photoelectron Spectroscopy Study of Cobalt Foil Model Catalyst under CO, H_2, and Their Mixtures. *ACS Catal.*, **2017**, 7, 1150 - 1157.

(26) Lee, A. F.; Lambert, R. M. Oxidation of Sn overlayers and the structure and stability of Sn oxide films on Pd(111). *Phys. Rev. B*, **1998**, 58, 7, 4156-4165.

(27) Santis, M. D.; Buchsbaum, A.; Varga, P.; Schmid, M. Growth of ultrathin cobalt oxide films on Pt(111). *Phys. Rev. B*, **2011**, 84, 125430.

(28) Walton, A. S.; Fester, J.; Bajdich, M.; Arman, M. A.; Osiecki, J.; Knudsen, J.; Vojvodic, A.; Lauritsen, J. V.; Interface Controlled Oxidation States in Layered Cobalt Oxide Nanoislands on Gold. *ACS Nano,* **2015**, 9, 3, 2445-2453.

(29) Risbud, A.; Snedeker, L. P.; Elcombe, M. M.; Cheetham, A. K.; Seshadari, R. Wurtzite CoO. *Chem. Mater.,* **2005**, 17, 834.

(30) Meyer, W.; Hock, D.; Biedermann, K.; Gubo, M.; Müller, S.; Hammer, L.; Heinz, K.; Coexistence of Rocksalt and Wurtzite Structure in Nanosized CoO Films. *Phys. Rev. Lett.,* **2008**, 101, 016103.

(31) Fester, J.; Sun, Z.; Rodríguez-Fernández, J.; Walton, A.; Lauritsen, J. V. Phase Transitions of Cobalt Oxide Bilayers on Au(111) and Pt(111): The Role of Edge Sites and Substrate Interactions. *J. Phys. Chem. B.,* **2018**, 122, 561 - 571.

(32) Fester, J.; García-Melchor, M.; Walton, A. S.; Bajdich, M.; Li, Z.; Lammich, L.; Vojvodic, A.; Lauritsen, J. V. Edge reactivity and water-assisted dissociation on cobalt oxide nanoislands. *Nat. Commun.,* **2017**, 8, 14169.

(33) Beitel, G. A.; Laskov, A.; Oosterbeek, H.; Kuipers, E. W. Polarization Modulation Infrared Reflection Absorption Spectroscopy of CO Adsorption on Co(0001) under a High-Pressure Regime. *J. Phys. Chem.,* **1996**, 100, 12494 - 12502.

(34) Ferstl, P.; Mehl, S.; Arman, M. A.; Schuler, M.; Toghan, A.; Laszlo, B.; Lykhach, Y.; Brummel, O.; Lundgren, E.; Knudsen, J.; Hammer, L.; Schneider, M. A.; Libuda, J. Adsorption and Activation of CO on Co_3O_4(111) Thin Films. *J. Phys. Chem. C,* **2015**, 119, 16688-16699.

(35) Wu, P.-Y.; Jiang, Y.-P.; Zhang, Q.-Y.; Jia, Y.; Peng, D.-Y.; Xu, W. Comparative study on arsenate removal mechanism of MgO and MgO/TiO_2 composites: FTIR and XPS analysis. *New J. Chem.,* **2016**, 40, 2878.

(36) Knudsen, J.; Martin, M. N.; Grånäs, E.; Blomberg, S.; Gustafson, J.; Andersen, J. N.; Lundgren, E.; Klacar, S.; Hellman, A.; Grönbeck, H. Carbonate formation on p(4x4)-O/Ag(111). *Phys. Rev. B,* **2011**, 115430.

(37) Hertl, W. Infrared Spectroscopic Study of Catalytic Oxidation Reactions Over Cobalt Oxide Under Steady-State Conditions. *J. Catal.,* **1973**, 31, 231-242.

(38) Eren, B.; Heine, C.; Bluhm, H.; Somorjai, G. A.; Salmeron, M. Catalyst Chemical State during CO Oxidation Reaction on Cu(111) Studied with Ambient-Pressure X-ray Photoelectron Spectroscopy and Near Edge X-ray Adsorption Fine Structure Spectroscopy. *J. Am. Chem. Soc.,* **2015**, 137, 11186 - 11190.

(39) Fester, J.; Sun, Z.; Rodríguez-Fernández, J.; Lauritsen, J. V. Structure of CoO_x Thin Films on Pt(111) in Oxidation of CO. *J. Phys. Chem. C,* **2019**, 123, 17407-17415.

(40) Ogletree, D. F.; Bluhm, H.; Hebenstreit, E. D.; Salmeron, M. Photoelectron spectroscopy under ambient pressure and temperature conditions. *Nucl. Instrum. Methods Phys. Res,* **2009**, 601, 151-160.

(41) Mars, P.; van Krevelen, D. W. Oxidations carried out by means of vanadium oxide catalysts. *Chem. Eng. Sci.,* **1954**, 3, 41-59.

(42) Longwitz, S. R.; Schnadt, J.; Vestergaard, E. K.; Vang, R. T.; Lægsgaard, E.; Stensgaard, I.; Brune, H.; Besenbacher, F. High-Coverage Structures of Carbon Monoxide Adsorbed on Pt(111) Studied by High-Pressure Scanning Tunneling Microscopy. *J. Phys. Chem. B,* **2004**, 108, 14497-14502.

(43) Kinne, M.; Fuhrmann, T.; Whelan, C. M.; Zhu, J. F.; Pantförder, J.; Probst, M.; Held, G.; Denecke, R.; Steinrück, H.-P. Kinetic parameters of CO adsorbed on Pt(111) studied by *in situ* high resolution x-ray photoelectron spectroscopy. *J. Chem. Phys.,* **2002**, 117, 23, 10852 - 10859.

(44) Xu, L.; Ma, Y.; Zhang, Y.; Chen, B.; Wu, Z.; Jiang, Z.; Huang, W.; Water Adsorption on a Co(0001) Surface. *J. Phys. Chem. C,* **2010**, 114, 17023 - 17029.

(45) Nagakura, S. Study of Metallic Carbides by Electron Diffraction Part IV. Cobalt Carbides. *J. Phys. Soc. Jpn.,* **1961**, 114, 17023-17029.

(46) Tuxen, A.; Carenco, S.; Chintapalli, M.; Chuang, C.-H.; Escudero, C.; Pach, E.; Jiang, P.; Borondics, F.; Beberwyck, B.; Alivisatos, A. P.; Thornton, G.; Pong, W.-F.; Guo, J.; Perez, R.; Besenbacher, F.; Salmeron, M. Size-Dependent Dissociation of Carbon Monoxide on Cobalt Nanoparticles. *J. Am. Chem. Soc.,* **2013**, 135, 6, 2273-22.

Supporting Information for

CO oxidation mechanisms on CoO$_x$-Pt thin films

Heath Kersell[1], Zahra Hooshmand[2], George Yan[7], Duy Le[2], Huy Nguyen[7], Baran Eren[1], Cheng Hao Wu[1], Iradwikanari Waluyo[3], Adrian Hunt[3], Slavomír Nemšák[4], Gabor Somorjai [1,5], Talat S. Rahman[2], Philippe Sautet[7,8], Miquel Salmeron[1,6]

[1]Chemical Sciences Division, Lawrence Berkeley National Laboratory, Berkeley, CA, 94720, USA

[2]Department of Physics, University of Central Florida, Orlando, Florida 32816, United States

[3]National Synchrotron Light Source II, Brookhaven National Laboratory, Upton, New York, 11973, USA

[4]Advanced Light Source, Lawrence Berkeley National Laboratory, Berkeley, California, 94720, USA

[5]Department of Chemistry, University of California, Berkeley, California, 94720, United States

[6]Department of Materials Science and Engineering, University of California, Berkeley, California, 94720, USA

[7] Department of Chemical and Biomolecular Engineering, University of California, Los Angeles, USA

[8] Department of Chemistry and Biochemistry, University of California, Los Angeles, USA

S1. XPS Peak Fitting and Further Experimental Procedures

X-ray photoelectron spectroscopy (XPS) data was evaluated by first referencing all binding energy scales to the Fermi edge collected for each spectrum and subtracting a Shirley background from the fine scan region in question (Co 2p, O 1s, C 1s, Pt 4f). The C 1s and O 1s spectra were fitted with Voigt–type line shapes for each peak. To avoid over-interpretation, the minimum number of peaks required to fit the spectral features were used, subject to constraints imposed by, e.g., FWHM of the elemental species or obvious shoulders indicating multiple features. Metallic components of the Co 2p region were fitted with a spectral profile characteristic of Co^0 using an asymmetric Lorentzian profile for the main peak using CasaXPS with the form LA(1.2,5,5). [1] Co 2p components arising from CoO, with the accompanying characteristic satellite structure, were fitted with symmetric Voigt–type peaks (as was the oxide peak in the O 1s region).

The fits of the metallic and oxide components of the Co 2p region were used to determine the initial composition of the CoO$_x$ films. The accuracy of this procedure depends on a number of parameters including the signal-to-noise ratio, quality and composition of the reference and measured samples, and quality of the fittings. The signal-to-noise ratio of the Co 2p spectra presented here is quite high, so statistical counting variations are not the limiting factor in the uncertainty of the composition analysis. Rather, comparability between the 2p spectra of our samples and the reference samples is more relevant. This was addressed by identifying conditions where our CoO$_x$ films were readily distinguished as predominantly Co^{2+} or Co^0, and

1 fitting the Co 2p profiles of reference CoO and Co^0 samples[1] to the 2p spectra of our samples at
2 those conditions. Then the peak positions and satellite structures for Co^{2+} and Co^0 could be
3 adjusted match to spectra measured on our samples. Distinction between Co^0, Co^{2+}, and Co^{3+} is
4 facilitated by the binding energy (BE), satellite structure, and spin splitting of each state. [1] [2]
5 [3] Since our samples may always contain a small
6 amount of Co^{2+} or Co^0, this procedure is prone to
7 some fitting uncertainty. We estimate the
8 uncertainty of the Co 2p compositional analysis
9 to be approximately 3.4%, although it may be
10 higher for spectra which are predominantly
11 comprised of Co^{2+} (as discussed in section S2).
12 Meanwhile, uncertainty in the O 1s peak areas
13 are more closely related to the XPS signal-to-
14 noise ratio. As a result, the lower limit for
15 detecting a reduction in the O 1s oxide peak
16 intensity was better than 1% of the peak area for
17 any spectrum considered in this work. Finally,
18 we note that some carbonate and carbide species
19 accumulate on the films as they are exposed to
20 CO. Since both species can affect the 2p
21 spectrum of Co, the O 1s oxide peak provides a
22 more accurate picture of the evolution of the
23 oxide.

24 During data acquisition it is necessary to
25 understand the effect of the X-ray beam on the
26 sample, and to prevent beam induced damage.
27 Beam damage can lead to changes in sample
28 composition and dissociation of adsorbates or gas
29 phase species. As an example, gas phase oxygen
30 can be dissociated, leading to reactions that do
31 not represent the chemical activity of the sample
32 without the beam. To minimize beam damage, all
33 XPS data shown in the main text was collected
34 with the X-ray shutter closed when data was not
35 actively being acquired. However, this only
36 reduces the beam exposure by less than one order
37 of magnitude. Hence, we also checked for beam
38 induced effects during experiments by moving
39 the sample and measuring XPS at a location that
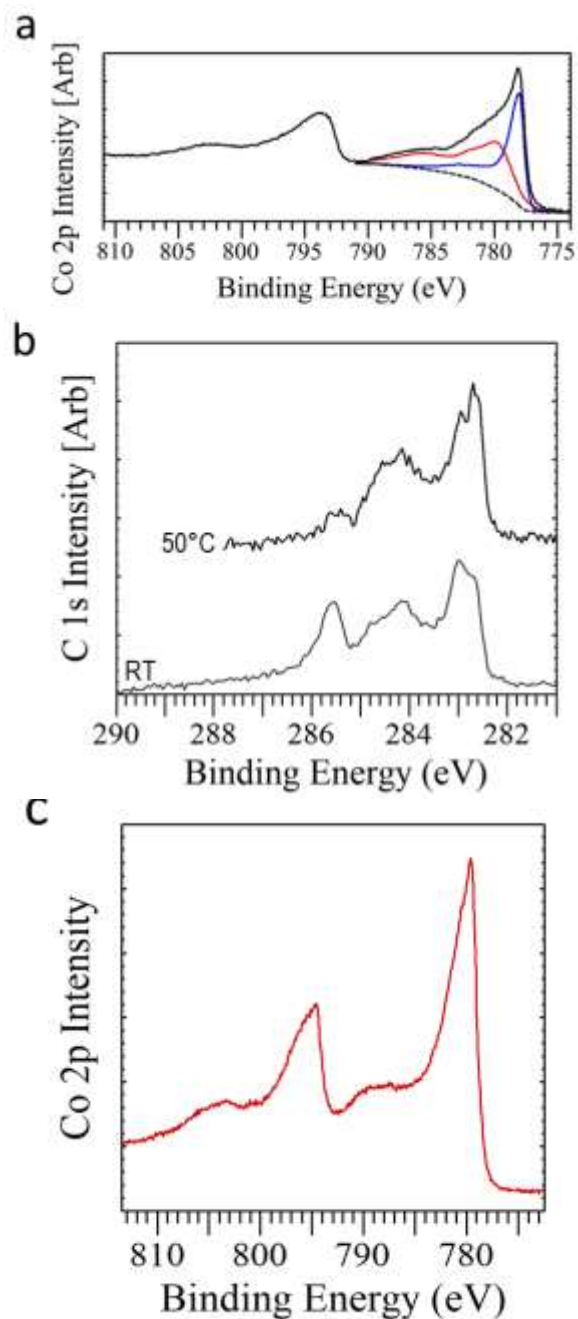40 had not yet been exposed to the beam. No

Figure S1: Temperature dependent sample properties. a) XPS Co 2p region of submonolayer CoO_x film prepared by exposure to 50 L O_2 at 60° C. The film contains ~55% Co^{2+}. b) The C 1s region recorded on 2 ML Co films deposited on Pt(111) before oxygen exposure. The films are initially observed at RT, and then heated to 50° C. c) The Co 2p region for a CoO_x film containing a mixture of Co^{2+} and Co^{3+}.

1 significant beam induced effects were observed between locations.

2

3

4

5

6 **S2. Temperature Dependence and Carbon Species**

7 Here, we provide data showing the dependence of the CoO_x-Pt behavior on heating. Fig.
8 S1a shows XPS in the Co 2p region for a submonolayer CoO_x film on Pt(111). The oxide was
9 formed by holding the sample at 60° C during exposure to 50 L of O_2. This changed the
10 composition to 55% Co^{2+}, compared with the 50% Co^{2+} found when submonolayer samples were
11 held at RT during O_2 exposure (Fig. 1b, main text, top spectrum).

12 Next, we provide a brief description of the XPS spectral features resulting from
13 adsorption of background gas and contaminant species. CO was present in the background gas in
14 the 10^{-10} Torr regime, and adsorbed on the Pt(111) substrates and the thin films grown on those
15 surfaces during the measurements. In the case of 2 ML films, prior to oxidation, this background
16 CO generated a CO/Co^0 peak at 285.6 eV (Fig. S1b). [2] Heating to just 50 °C caused the area of
17 this peak to decrease, characteristic of CO desorption from metallic Co. Three other features
18 appeared in the C 1s spectra under the same conditions. Peaks at 282.7 eV and 283 eV are
19 attributed to carbidic C formed upon Co deposition, with the differing positions resulting from
20 the formation of carbide species with different stoichiometries. [2] [3] [4] [5] Interestingly, these
21 carbide peaks vanished upon exposing the surface to 5000 L O_2 at 60 °C (Fig. 2a, main text,
22 spectrum (1)). Carbonaceous species, CH_x, generate a peak just above 284 eV. Here, the broad
23 nature of this feature indicates that more than one species is present. Indeed, structural
24 differences in such carbon species can yield different binding energies for these features. [6]

25 Finally, as mentioned in section S1, oxides containing Co^{3+} can be formed at higher O_2
26 pressures and temperatures. The most common of these is Co_3O_4, a mixture of Co^{2+} and Co^{3+}. [1]
27 Fig. S1c shows the Co 2p region for a CoO_x film heated to 280 °C in 40 mTorr of O_2, which
28 contains a mixture of Co^{2+} and Co^{3+}. 2p spectra of Co^{3+} have a different combination of satellite
29 structure, peak position, and spin splitting than Co^0 or Co^{2+}. [1] [2] [3] While such mixtures can
30 be clearly distinguished from Co^{2+} and Co^0, the distinction between Co^{2+} and Co^{3+} is not trivial
31 for some mixtures of these two states, especially in films containing only a few percent Co^{3+}. The
32 strength of the spin splitting between the Co $2p_{3/2}$ and Co $2p_{1/2}$ peaks is significantly higher in
33 Co^{2+} than in Co^0 and Co^{3+}. This provides a further mechanism for distinguishing Co^{2+} from Co^{3+}.
34 Nevertheless, aside from the spectrum in Fig. S1c, no film shown in this work had a Co 2p
35 spectrum containing features clearly characteristic of Co^{3+}, and all but the top spectrum in Fig.
36 1a contain a clear contribution from Co^0.

37

38 **S3. Carbonate Formation on 2.8 ML Films**

39 Fig. S2 shows the C 1s region on a 2.8 ML film under various conditions. This is the
40 same film that produced the spectra in Fig. 4 of the main text. Initially in UHV, after exposure to

1   5 L O_2, only a small amount of carbon contaminant species were present on the film. When the

2   oxide was reduced in 140 mTorr CO (main text, Fig. 4b), little or no carbonate formed (Fig. S2).

3   Adding O_2 to the gas mixture, in a 1:2 ratio of O_2:CO, caused CO to cease adsorbing on Co^0 and

4   instead to form carbonate species which are stable at RT, as shown in Fig. 2 of the main text.

5   **S4. Carbonate Formation and Irreducibility of CoO Films**

6   In conditions where carbonate forms on CoO_x films, the oxide is no longer reduced by

7   CO exposure at RT. To demonstrate this, Figure S3 shows the intensity of the cobalt oxide peak

8   at 529.3 eV as a function of gas pressure and composition for a submonolayer CoO_x film. This

9   film was formed using the same procedure that generated the data in Figures 6 and 7 of the main

10   text, and contained exposed O vacancies. The gas composition in each section of the plot is

11   indicated at the top of the figure. Initially, the film was measured in increasing CO pressures

12   from UHV up to 140 mTorr, whereupon the oxide peak intensity decreased (left CO region).

13   Afterwards, 70 mTorr O_2 was added to the gas mixture (CO+O_2 region). Under these conditions,

14   the film becomes more oxidized and CO adsorbs as carbonate (e.g. Fig. S2 and Fig. 7). Finally,

15   the CO+O_2 gas mixture was pumped away to UHV, and 140 mTorr CO was then added back

16   into the chamber (right section). After carbonate formation, the CoO film was no longer reduced

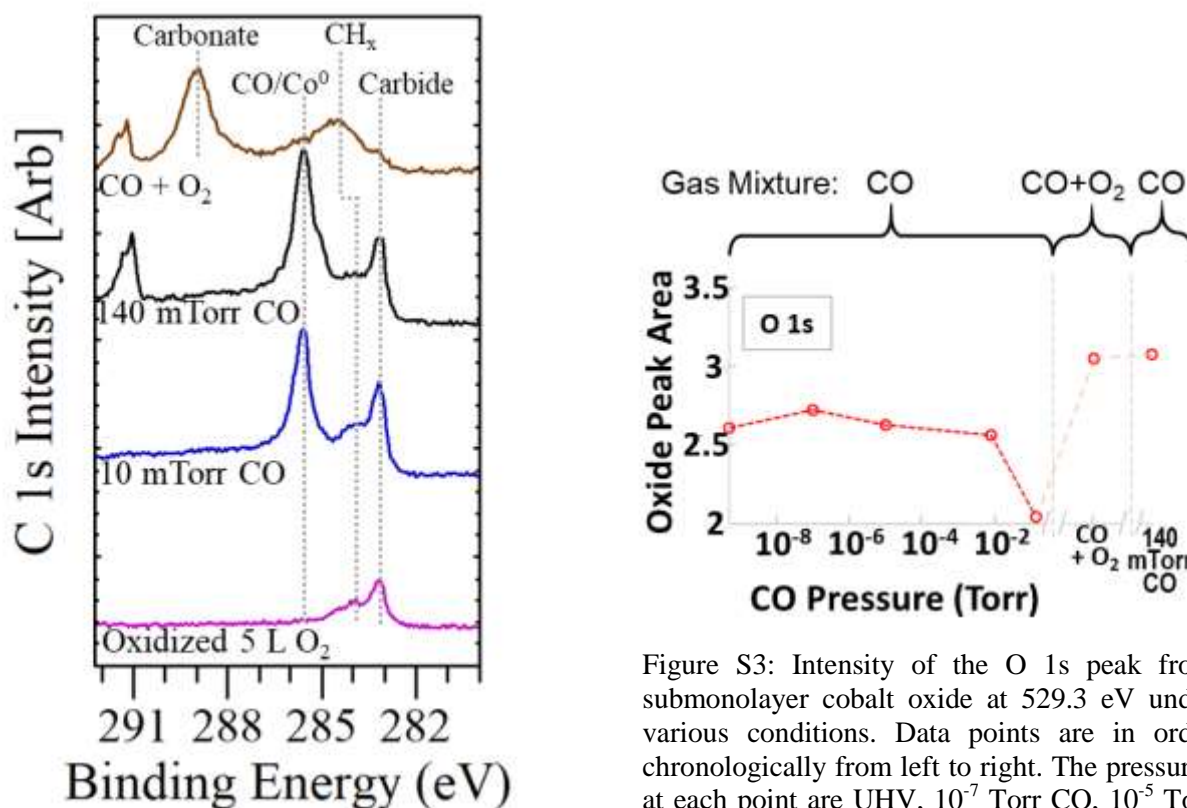17   by the same CO exposure at RT that had previously reduced it.

Figure S2: C 1s region recorded under various conditions on a 2.8 ML film prepared by exposure to 5 L O_2. The film is initially in UHV (bottom spectrum), and is exposed to higher CO pressures and gas mixtures.

Figure S3: Intensity of the O 1s peak from submonolayer cobalt oxide at 529.3 eV under various conditions. Data points are in order chronologically from left to right. The pressures at each point are UHV, 10^{-7} Torr CO, 10^{-5} Torr CO, 10 mTorr CO, 140 mTorr CO, 140 mTorr CO + 70 mTorr O_2, and 140 mTorr CO. For the last measurement on the right, the CO + O_2 gas mixture shown in the 'CO + O_2' region was pumped away, and 140 mTorr CO was added back into the chamber.

1

2

S5. Further Discussion of Oxidized Co Films

When Co films of just one atomic layer thickness were exposed to 50 L O_2 at RT, they were only partially oxidized into CoO (as shown in the main text, Fig. 1b), with some metallic Co remaining at the surface. Under these conditions, a hexagonal structure with 1 nm spacing was observed on all single layer films, regardless of the coverage of the first layer (Fig. 1f,g).

We note that ordered monolayer CoO films with 3.09 Å atomic periodicity were previously grown by De Santis et al. [7]. Those films contained a Moiré pattern similar to that shown in Fig. 1d (main text), indicating a more fully oxidized surface. We also prepared submonolayer films oxidized by 50 L O_2, the same O_2 exposure that produced the submonolayer films discussed in the main text, but with the sample held at 60° C during oxidation. This increased the fractional CoO composition in the films to 59%, still lower than for the 2 ML CoO films oxidized under the same conditions.

In the case of the 2 ML films shown in Fig. 1c,d of the main text, the 3.4 Å spacing is similar to that for surface layers of wurtzite CoO, whose bulk lattice constant of 3.244 Å [8] expands to 3.476 Å at the surface. Meanwhile, the lattice constant in the case of the films grown by De Santis et al. suggests a rocksalt phase. [7] Bridging these observations, Meyer et al. showed that CoO films as thin as 1 nm assume a mixed structural state where a registry shift at the top few layers leaves the surface with a wurtzite structure, while the underlying layers assume the rocksalt phase. [9]

S6. Density Functional Theory

For the DFT calculations, we performed two separate sets of calculations using the Vienna ab-Initio Simulation Package (VASP), and projector-augmented wave and plane wave basis set methods. In both cases, the Perdew-Burke-Ernzerhof functional was used to calculate the exchange-correlation energy. One set of calculations employed spin-polarized DFT (SP-DFT) to understand the behavior of CoO films interacting with CO and O_2. The other approach included a Hubbard-like repulsion term due to the strong self-interaction of the Co 3d electrons, and was used to study partially oxidized CoO_x films. Both approaches yielded qualitatively similar results for calculations of the same processes (e.g. CO interacting with CoO film (island) interiors as described in the main text). The SP-DFT calculations were employed to study the behavior of CO and O_2 interacting with both isolated lattice oxygen vacancies in CoO islands, and with CoO island edge sites. Meanwhile, the DFT+U calculations accounted for the presence of gas phase reactants by considering entropic contributions to the behavior of reactant and product species, were used to study the behavior of partially oxidized CoO films comprised of 50% CoO, in an attempt to replicate the experimental conditions as closely as possible. Further details of each approach are provided in the following.

39

1 **S6a. SP-DFT: Additional details of calculations**

2   For the SP-DFT calculations, the kinetic energy cutoff was set to 500 eV and the
3 Brillouin Zone was sampled using 1×2×1 k-point mesh. To find the minimum energy of the
4 systems, all the atoms were allowed to move until the force acting on each atom was less than
5 0.03 eV/Å in all directions. A vacuum of 27 Å was set between the perpendicular images of
6 simulation unit cells to avoid the interaction between them. The adsorption energies were
7 calculated using the following equation:

8      $$E_{ads} = E[CO + CoO/Pt(111)] - E[CO(g)] - E[CoO/Pt(111)],$$

9

10 where $E[CO + CoO/Pt(111)]$ is the total energy of CO adsorption on the sub-monolayer of CoO
11 on Pt(111), $E[CO(g)]$ is the total energy of CO in the gas phase and $E[CoO/Pt(111)]$ is the total
12 energy of clean submonolayer CoO on Pt(111). Due to the large supercell used in our
13 calculations, calculation of reaction barriers directly from Nudged Elastic Band method [10, 11]
14 is not economical. Instead, we estimate the barriers for CO to approach the edge and interior sites
15 of submonolayer CoO by calculating the potential energy profile of CO above the O atom of the
16 island edge and interior sites with distances from 5.5 Å to 1.5 Å with 0.5 Å steps. In these
17 calculations the C atom was kept fixed while all the other atoms were allowed to move.

18

19 *(i) Calculating the Termination of Submonolayer CoO on Pt(111)*

20   The edge site termination of submonolayer CoO was identified by examining two
21 different terminations, zig-zag and arm-chair (Fig. S4). The free energy calculations show that
22 arm-chair termination is favorable by an energy difference of 2.54 eV.
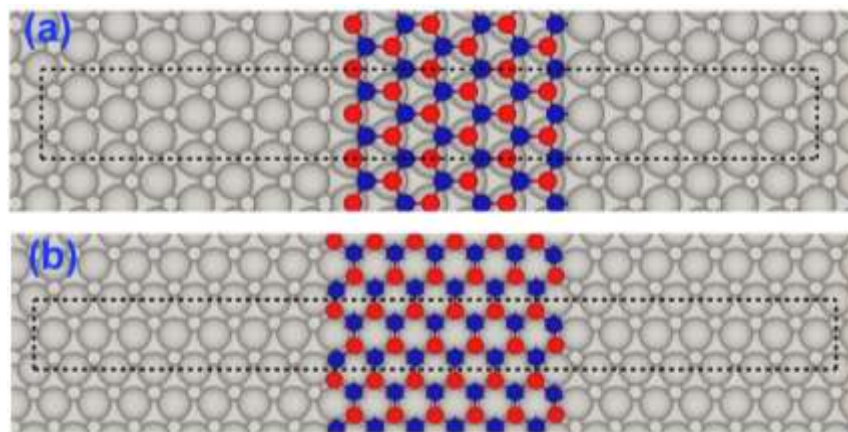
23 Figure S4. CoO terminations on Pt(111). (a) zig-zag termination and (b) arm-chair. Dotted lines show the
24 unit cell used to find the CoO termination. Color code of atoms: Grey - Pt, Dark Blue - Co and Red - O.

25

26 *(ii) Calculation of CO reaction with submonolayer CoO on Pt(111)*

27   To find the reaction mechanism of CO on submonolayer CoO over Pt(111), the
28 adsorption energies of CO on all the possible adsorption sites were investigated. Figure S5 shows
29 these sites on the submonolayer CoO/Pt(111) supercell, and Table S1 shows the adsorption
30 energy for CO on each site. Based on these calculations, the interaction of CO with CoO edges

takes place either by making a bond with edge Co or O atoms. However, it is strongest when interacting with O atoms, which leads to spontaneous CO oxidation and leaves an O vacancy on the edge. At CoO interior sites, on the other hand, CO can adsorb weakly between two oxygen atoms to form a carbonate structure (Figure S5c, Table S1). When CO is positioned on an interior lattice O atom (Fig. S5d), CO oxidation takes place and leaves an oxygen vacancy behind as on the edges, with an adsorption energy of over 1 eV higher than for carbonate formation. On the three-fold hollow (TFH) site (Fig. S5a), among three Co atoms, CO does not make a bond and instead moves away from the surface. On a Co atom (Fig. S5b), at a site between three lattice O atoms, although CO pulls the Co atom up from the surface, the adsorption energies show that, this adsorption is endothermic.
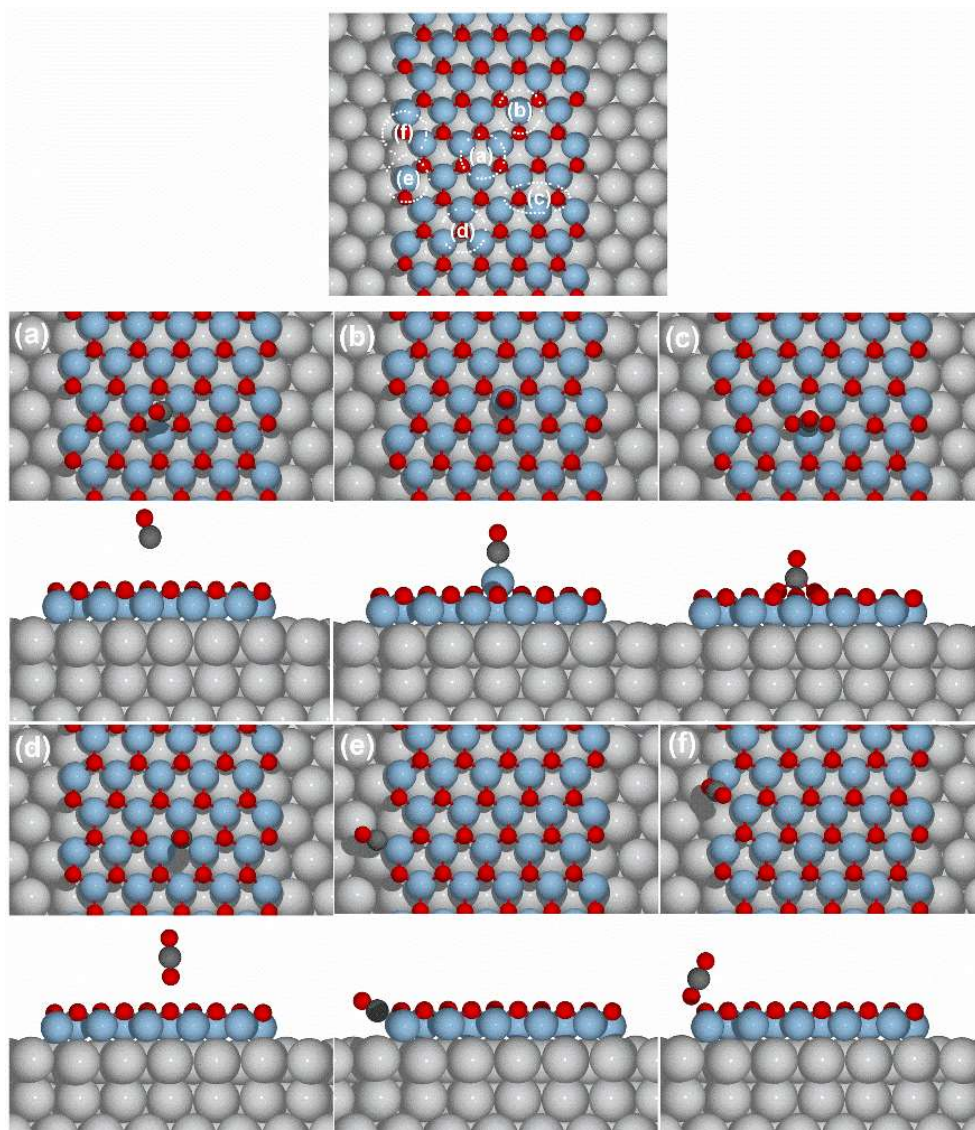
Figure S5. Top: Possible adsorption sites for CO on submonolayer CoO films on Pt(111). (a-f) top and side views of final adsorption configuration of CO on submonolayer CoO films on Pt(111). Color code of atoms: Pt (grey), Co(blue), O(Red) and C(dark-grey).

System	Adsorption Energy(eV)
(a)	0.016
(b)	0.23
(c)	-0.067
(d)	-1.05
(e)	-1.21
(f)	-1.60

Table S1. Adsorption energies of CO for systems shown in Figure S5(a-f).

1   After CO oxidation creates a single O vacancy site on the interior of CoO sub-monolayer
2   films, CO can adsorb on either the vacancy site or on the O atoms nearby the vacancy. We
3   obtained the adsorption energy for CO on the vacancy, as shown in Fig. S6(b), as -1.35 eV.
4   Meanwhile, on the O atoms adjacent to the vacancy, the adsorption energy is -2.39 eV, shown in
5   Fig. S6(c). Therefore, the latter is energetically more favorable than the former. This reaction, as
6   shown in Fig. S6(c) removes another O atom, creating more O vacancies on the interior of
7   submonolayer CoO islands.
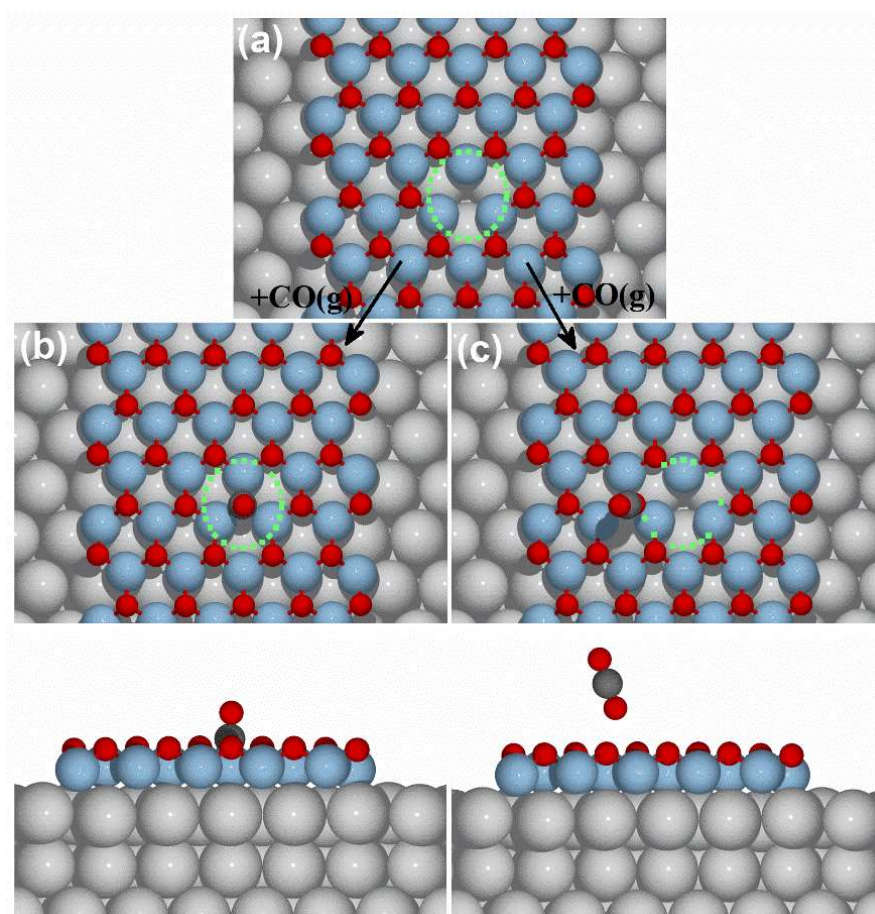
8   Figure S6. Reaction of CO on the O vacancy site inside submonolayer CoO islands. (a) dotted green
9   circle shows the single O vacancy site. (b) adsorption of CO on the O vacancy site and (c) adsorption of
10   CO on the O atoms nearby the vacancy site. Color code of atoms: Pt (grey), Co(blue), O(Red) and
11   C(dark-grey).
12

13   Another possible reaction on the single O vacancy site inside the CoO sub-monolayer
14   islands is adsorption of O_2. This reaction lowers the energy of the system by 2.19 eV. The
15   configuration of O_2 on the vacancy site is shown in Fig. S7(b). The consequent adsorption of CO
16   on this site removes one of the O atoms by formation of CO_2 and the remaining O atom heals the
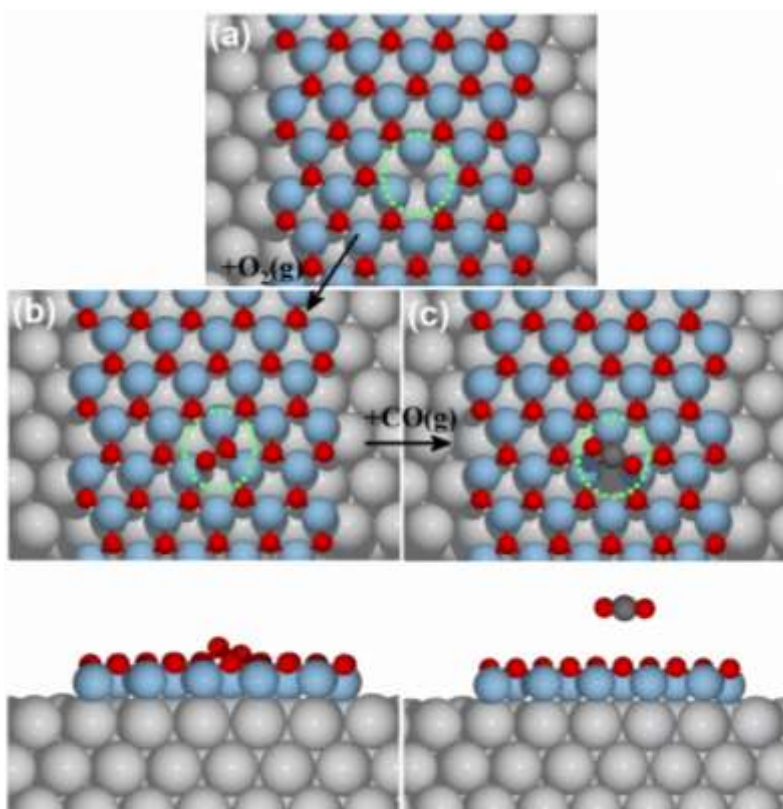17   vacancy (Fig. S7(c)).
18

Figure S7. Reaction O_2 and CO on the O vacancy site inside the submonolayer CoO islands. (a) dotted green circle shows the single O vacancy site. (b) adsorption of O_2 on the O vacancy site and (c) CO oxidation on the atomic $2O^*$. Color code of atoms: Pt (grey), Co(blue), O(Red) and C(dark-grey).

S6b. DFT+U: Additional details of calculations

Periodic density functional theory (DFT) calculations were performed using the Vienna ab-Initio Simulation Package. [12, 13, 14] The PAW method was used to describe electron-core interactions. [15] A basis set of plane waves with kinetic energy up to 500 eV was used to develop the one-electron wavefunctions for the half-oxidized $CoO_{0.5}$/Pt(111), while a set of plane waves with kinetic energy up to 450 eV was used for the fully-oxidized CoO/Pt(111). The Brillouin zone was sampled using a (3 x 3 x 1) and a (5 x 5 x 1) Monkhorst-Pack mesh for the ($2\sqrt{3}$ x $2\sqrt{3}$) and (2 x 2) cells, respectively. [16] Based on investigations of single-layer CoO and FeO films in the literature, a row-wise antiferromagnetic structure was maintained for all the structures in the DFT+U calculations. [17]

The Perdew-Burke-Ernzerhof functional was used to calculate the exchange-correlation energy. [18] A Hubbard-like repulsion term (U) was used in these calculations by the method of Dudarev et al., due to the strong self-interaction of the Co 3d electrons. [19] The PBE+U calculations were performed using U_{eff} = 3.5 eV; this value of U_{eff} has been shown to reliably reproduce the redox properties of Co_3O_4. [20] Since CO from the gas phase physisorbs weakly to initiate reaction with surface O, the dDsC dispersion correction was used to describe the van der Waals (vdW) forces left out by the PBE functional. [21, 22] The transition states were first optimized by the climbing-image nudged elastic band method. [11, 10] Next, the highest-energy

1 image was optimized by the dimer method. [23] Finally, the transition state geometry was
2 optimized using the quasi-Newton method. All geometries were converged until forces are below
3 0.05 eV/Å. The Gibbs free energy is approximated by adding the translational and rotational
4 degrees of freedom of gas phase CO and CO_2 to the energies of CO and CO_2. [24] 303 K was used
5 as the temperature of the system. 144 mTorr was used as the pressure of CO, and 3 x 10^{-10} Torr
6 was used as the pressure of CO_2.

7
8

9 *(i) CoO$_x$/Pt(111) Structures*
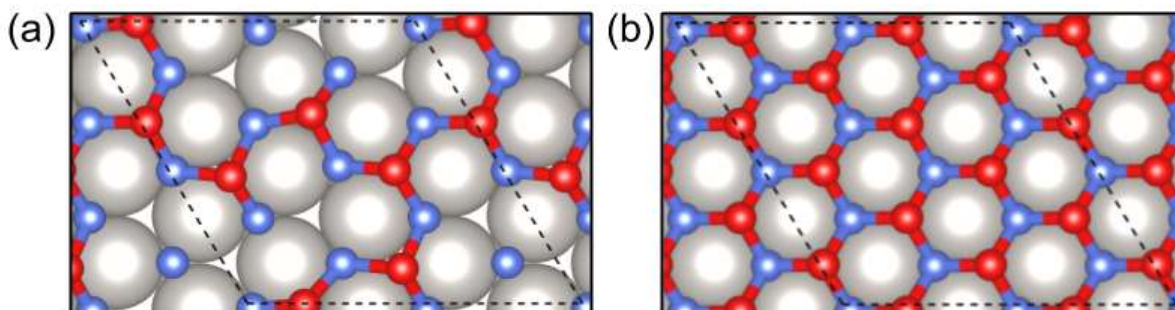
Figure S8. Geometry of the types of CoO$_x$/Pt(111) structures studied: (a) top view of the fully-oxidized single-monolayer CoO/Pt(111) structure in a (2√3 x 2√3) cell (colors: Pt: gray, O: red, Co: blue); (b) half oxidized model surface CoO$_{0.5}$/Pt(111), in order to simulate the XPS-detected degree of reduction. A third type of surface was constructed by subjecting the fully-oxidized epitaxial one-monolayer CoO/Pt(111) in a (2√3 x 2√3) cell (a) to strain. Specifically, the Pt-Pt distance (and hence also the Co-Co distance) were expanded to 3.15 Å.

10

11   In the DFT+U calculations, we built three types of models by stacking CoO epitaxially
12 on top of the Pt lattice (Fig. S8). The first type was constructed by forming an epitaxial CoO
13 layer on Pt(111) (Fig. S8a). The second type, the half-oxidized CoO/Pt surface, is constructed by
14 removing half of all surface O from the fully-oxidized monolayer CoO/Pt surface (Fig. S8b). The
15 pattern of surface O atoms observed in the STM image (Fig. 1f,g) is replicated here, where
16 surface O atoms are arranged as thin lines (in accordance with thin dark lines in Fig. 1f,g)
17 bordering patches of exposed Co (in accordance with large bright spots in Fig. 1f,g).
18 Realistically, the CoO lattice is larger than that of the Pt substrate, which results in a long-range
19 Moire pattern too large to compute. To capture the effects of this expanded lattice, we
20 constructed a third model, where the fully-oxidized CoO/Pt surface (Fig. S8a) is strained.
21 Specifically, we increased the Pt-Pt distance (and hence also the Co-Co) to 3.15 Å and examined
22 the reactivity of this fully oxidized CoO surface with the Co-Co distance experimentally
23 observed.

24 *(ii) Interaction of CO with Various CoO$_x$ Surfaces*

1   Upon introducing CO to the fully-oxidized monolayer CoO/Pt(111) surface, we find that
2   CO weakly physisorbs on Co, and prefers to adsorb at the top and bridge sites of O to form CO_2
3   and CO_3^{2-}, respectively. Specifically, starting from the gas phase, CO adsorbs atop surface O to
4   form CO_2 through an energy barrier of 0.49 eV (or 1.23 eV free energy). The transition state
5   shows a CO unit tilted 120° from the vertical direction. The adsorbed CO_2 can have two
6   directions to proceed. Firstly, it can go through a small barrier of 0.61 eV whose transition state
7   is CO leaning toward a nearby O to form carbonate. Although the energy barrier can be
8   overcome at RT, the fact that carbonate is 0.33 eV less stable than the CO_2 makes this pathway
9   not favorable. Alternatively, CO can directly desorb into the gas phase. Although CO_2 is weakly
10 bound to the surface, its additional entropy in the gas phase facilitates the desorption, making the
11 overall reaction highly exergonic. Therefore, CO prefers to react to form CO_2 and desorb,
12 leaving behind an O vacancy. This reaction is exergonic with a net Gibbs free energy change of -
13 3.41 eV at the reaction conditions (Fig. S9). The free energy barrier is however 1.23 eV, so that
14 the reaction would be very slow at room temperature.
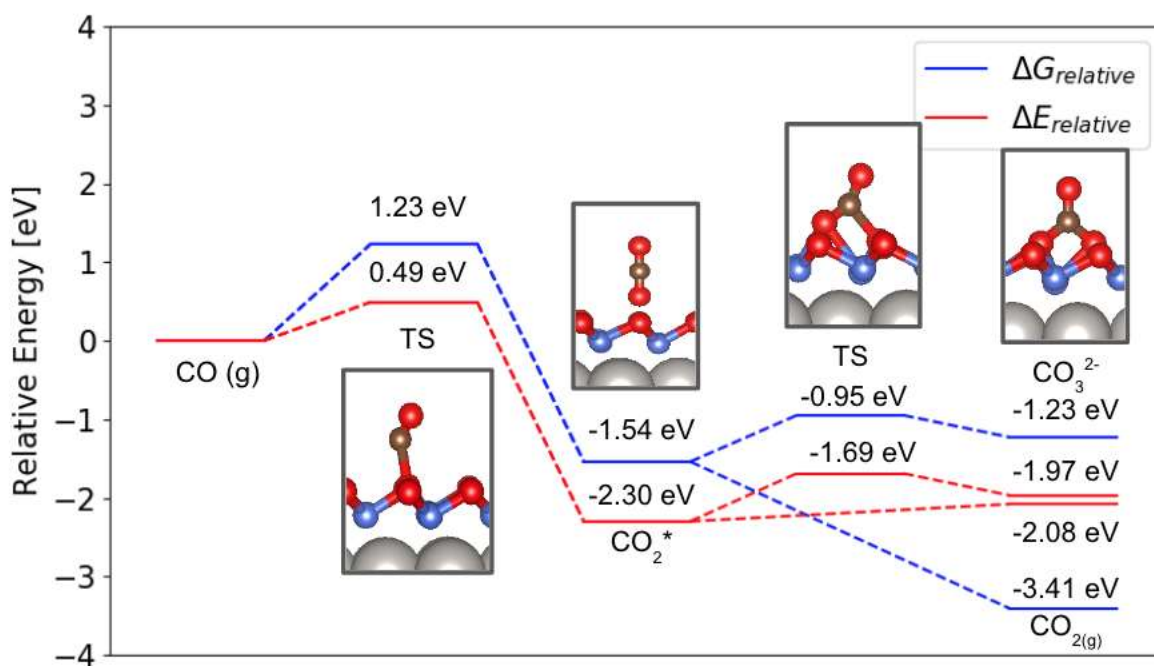
15
16 **Figure S9.** Reactivity of the fully oxidized monolayer CoO for the formation of CO_2 and CO_3^{2-}.
17 Energetically, making CO_2 is most favorable. TS stands for Transition State. The blue (resp. red) line
18 corresponds to the ΔG (resp. ΔE) profile. Note that taking into account temperature effect and free energy
19 is very important.

20   Furthermore, because Co is easily hydroxylated by background water during the
21 experimental setups, we also investigated the effects of OH groups to the surface reactions. We
22 modeled the OH group as a hydrogen atom adsorbed on surface O. Due to the addition of a
23 hydrogen atom, there are different configurations of carbonate species. Their isomerization is
24 shown in Fig. S10. Starting from carbonate, the nearby H can migrate to the carbonate O to form
25 bicarbonate. The barrier of this process is 0.68 eV, and the resultant species is almost as stable as

1   the former one. Furthermore, the bicarbonate can transform to the monodentate configuration in
2   a barrierless process. Because the difference in energy between isomers are small, we can expect
3   to have multiple carbonate species on the surface.
4
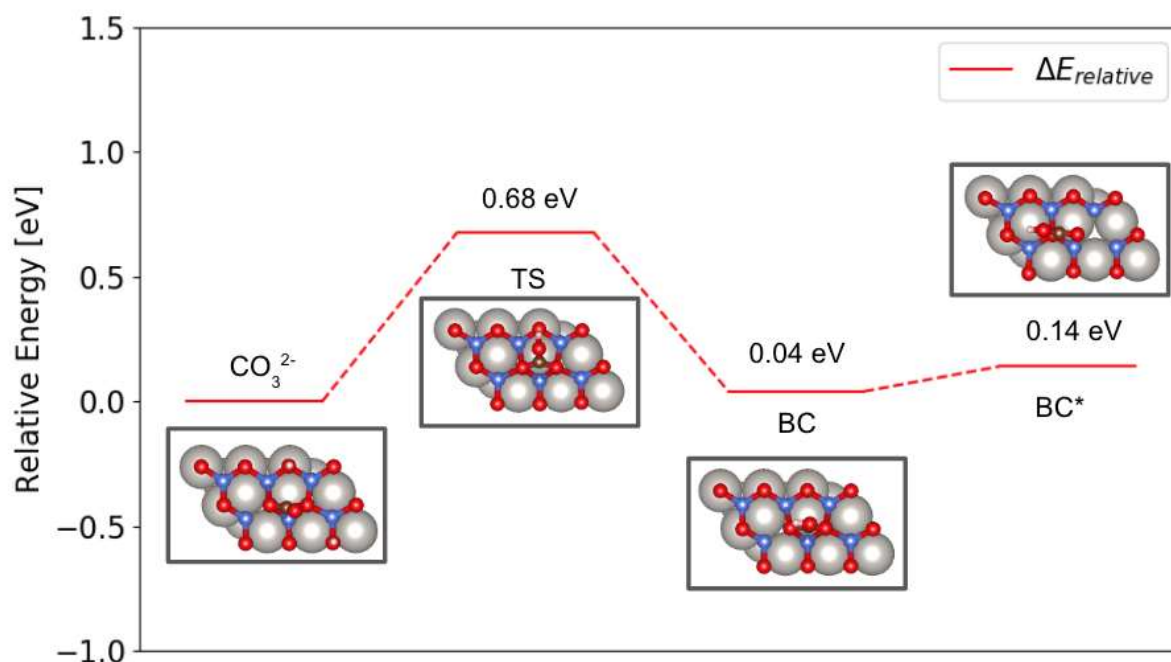
5
6   **Figure S10**. Isomerization of Carbonate species on the hydroxylated surface. Abbreviation: TS
7   (Transition State), BC (Bicarbonate), BC* (Monodentate Bicarbonate).

8

9   Similar CO behaviors happen on the expanded-lattice monolayer CoO surface.
10   Specifically, CO still prefers to form CO_2 and leaves behind an O vacancy. However, expanding
11   the lattice reduces the reaction energies (Table S2). For direct comparison, the reaction energies
12   of CO_2 and CO_3^{2-} for the (2x2) unexpanded cell are also included. In both surfaces, CO_2 is more
13   favorable than Carbonate by 0.2 eV. It is also evident that by increasing the distance between
14   atoms, each reaction energy drops by 0.6 eV. One explanation for this behavior is that expanded
15   cell is less stable than the unexpanded version.

16

17

	Unexpanded Surface		Expanded Surface	
	CO_2	CO_3^{2-}	CO_2	CO_3^{2-}
ΔE_{rxn} (eV)	-2.19	-1.98	-1.57	-1.36

ΔG_{rxn} (eV)	-1.45	-1.24	-0.83	-0.62

Table S2. Reactivity of the fully oxidized monolayer CoO with an expanded lattice (Pt-Pt distance of 3.15 Å) and unexpanded one (Pt-Pt distance of 2.78 Å) for the formation of CO_2 and CO_3^{2-}. The CO coverage is 0.25 in both cases. Energetically, the CO_2 is preferred.

On the other hand, for the half-oxidized CoO/Pt surface, we find that CO adsorbs exothermically atop exposed Co (Fig. S11a). On the free energy profile (blue), the surface reaction between lattice O and CO/Co (Fig. S11a) is preferred (with a free energy barrier of 0.87 eV) over the direct reaction between surface O and physisorbed CO (free energy barrier of 1.46 eV) (Fig. S11b). Energetically, forming CO_3^{2-} was found to be preferable to forming CO_2, but CO_2 formation and desorption is favored entropically on the ΔG surface.

Although the electronic energy barriers to form CO_2 and CO_3^{2-} by directly reacting gas phase CO on surface O are lower than that of the surface reaction between CO and O (Fig. S11a), too much entropy is lost when directly performing the reaction between gas and surface, resulting in a large initial free energy barrier. Thus, under the experimental conditions, CO oxidation on the terraces proceeds through a surface reaction from CO adsorbed on non-oxidized Co atoms. This also explains why the partially oxidized $CoO_{0.5}$ surface is more reactive that the fully oxidized one, where CO chemisorption is not possible (free energy barrier of 0.87 eV for $CoO_{0.5}$ in figure S11b, versus 1.23 eV for CoO in figure S9).
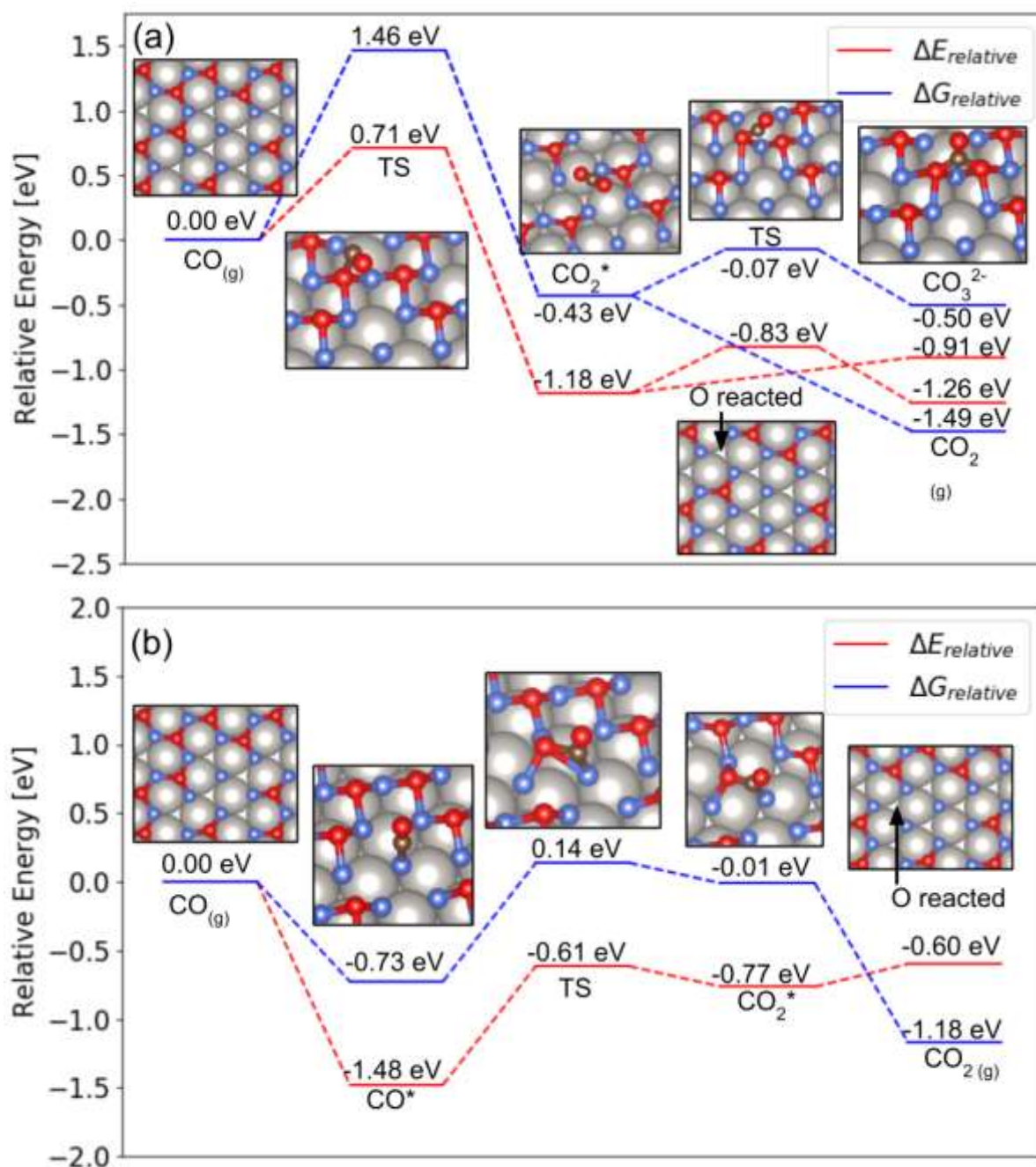
Figure S11 (duplicated from Figure 10a, b from the main text). Reactivity of the sub-oxidized monolayer $CoO_{0.5}$ for (a) the CO surface reaction to form CO_2 and (b) the direct formation of CO_2 and CO_3^{2-} from CO in the gas phase.

S8 References

[1] M. C. Biesinger, B. P. Payne, A. P. Grosvenor, L. W. M. Lau, A. R. Gerson and R. S. Smart, "Resolving surface chemical states in XPS analysis of first row transition metals, oxides, and hydroxides: Cr, Mn, Fe, Co and Ni," *Appl. Surf. Sci.,* vol. 257, pp. 2717-2730, 2011.

[2] T. Ivanova, A. Naumkin, A. Sidorov, I. Emerenko and M. Kiskin, "X-ray photoelectron spectra and electron structure of polynuclear cobalt complexes," *J. Electron Spectrosc.,* Vols. 200-2003, pp. 156-

158, 2007.

[3] D. C. Frost, C. A. McDowell and I. S. Woolsey, "X-ray photoelectron spectra of cobalt compounds," *Mol. Phys.,* vol. 27, no. 6, pp. 1473-1489, 1974.

[4] C. H. Wu, B. Eren, H. Bluhm and M. B. Salmeron, "Ambient-Pressure X-ray Photoelectron Spectroscopy Study of Cobalt Foil Model Catalyst under CO, H2, and Their Mixtures," *ACS Catal.,* vol. 7, pp. 1150 - 1157, 2017.

[5] D. A. Wesner, G. Linden and H. P. Bonzel, "Alkali Promotion on Cobalt: Surface Analysis of The Effects of Potassium on Carbon Monoxide Adsorption and Fischer-Tropsch Reaction," *Appl. Surf. Sci.,* vol. 26, pp. 335-356, 1986.

[6] G. A. Beitel, A. Laskov, H. Oosterbeek and E. W. Kuipers, "Plarization Modulation Infrared Reflection Absorption Spectroscopy of CO Adsorption on Co(0001) under a High-Pressure Regime," *J. Phys. Chem.,* vol. 100, pp. 12494 - 12502, 1996.

[7] S. Nagakura, "Study of Metallic Carbides by Electron Diffraction Part IV. Cobalt Carbides," *J. Phys. Soc. Jpn.,* vol. 16, no. 6, pp. 1213 - 1219, 1961.

[8] M. Morkel, V. V. Kaichev, G. Rupprechter, H.-J. Freund, I. P. Prosvirin and V. I. Bukhtiyarov, "Methanol Dehydrogenation and Formation of Carbonaceous Overlayers on Pd(111) Studied by High-Pressure SFG and XPS Spectroscopy," *J. Phys. Chem. B,* vol. 108, pp. 12955 - 12961, 2004.

[9] M. D. Santis, A. Buchsbaum, P. Varga and M. Schmid, "Growth of ultrathin cobalt oxide films on Pt(111)," *Phys. Rev. B,* vol. 84, p. 125430, 2011.

[10] A. Risbud, L. P. Snedeker, M. M. Elcombe, A. K. Cheetham and R. Seshadari, *Chem. Mater.,* vol. 17, p. 834, 2005.

[11] W. Meyer, D. Hock, K. Biedermann, M. Gubo, S. Müller, L. Hammer and K. Heinz, "Coexistence of Rocksalt and Wurtzite Structure in Nanosized CoO Films," *Phys. Rev. Lett.,* vol. 101, p. 016103, 2008.

[12] G. Henkelman, B. P. Uberuaga and H. Jónsson, "A climbing image nudged elastic band method for finding saddle points and minimum energy paths," *J. Chem. Phys.,* vol. 113, no. 22, pp. 9901-9904, 2000.

[13] G. Henkelman and H. Jónsson, "Improved tangent estimate in the nudged elastic band method for finding minimum energy paths and saddle points.," *J. Chem. Phys.,* vol. 113, no. 22, pp. 9978-9985, 2000.

[14] G. Kresse and J. Furthmüller, "Efficiency of Ab-Initio Total Energy Calculations for Metals and Semiconductors Using a Plane-Wave Basis Set," *Comput. Mater. Sci.,* vol. 6, no. 1, pp. 15-50, 1996.

[15] G. Kresse and J. Hafner, "Ab Initio Molecular Dynamics for Liquid Metals," *Phys. Rev. B,* vol. 47, no. 1, pp. 558-561, 1993.

[16] G. Kresse and J. Furthmüller, "Efficient Iterative Schemes for Ab Initio Total-Energy Calculations Using a Plane-Wave Basis Set," *Phys. Rev. B,* vol. 54, no. 16, pp. 11169-11186, 1996.

[17] D. Joubert, "From Ultrasoft Pseudopotentials to the Projector Augmented-Wave Method," *Phys. Rev. B,* vol. 59, no. 3, pp. 1758-1775, 1999.

[18] J. D. Pack and H. J. Monkhorst, ""Special Points for Brillouin-Zone Integrations"-a Reply," *Phys. Rev. B,* vol. 16, no. 4, pp. 1748-1749, 1977.

[19] L. Giordano, G. Pacchioni, J. Goniakowski, N. Nilius, E. D. L. Rienks and H.-J. Freund, "Interplay between structural, magnetic, and electronic properties in a-FeO∕Pt(111)ultrathin film," *Physical Review B,* vol. 76, p. 075416, 2007.

[20] J. P. Perdew, K. Burke and M. Ernzerhof, "Generalized Gradient Approximation Made Simple," *Phys. Rev. Letters,* vol. 77, no. 18, pp. 3865-3868, 1996.

[21] S. Dudarev, G. Botton, S. Y. Savrasov, C. J. Humphreys and A. P. Sutton, "Electron-Energy-Loss Spectra and the Structural Stability of Nickel Oxide: An LSDA+U Study," *Phys. Rev. B,* vol. 57, no.

3, pp. 1505-1509, 1988.

[22] L. Wang, T. Maxisch and G. Ceder, "Oxidation Energies of Transition Metal Oxides within the GGA+U Framework," *Phys. Rev. B,* vol. 73, no. 19, pp. 1-6, 2006.

[23] S. N. Steinmann and C. A. Corminboeuf, "A Generalized-Gradient Approximation Exchange Hole Model for Dispersion Coefficients," *J. Chem. Phys.,* vol. 134, no. 4, p. 044117, 2011.

[24] S. N. Steinmann and C. Corminboeuf, "Comprehensive Benchmarking of a Density Dependent Dispersion Correction," *J. Chem. Theory Comput.,* vol. 7, no. 11, pp. 3567-3577, 2011.

[25] G. Henkelman and H. Jonsson, "Improved tangent estimate in the nudged elastic band method for finding minimum energy paths and saddle points," *J. Chem. Phys.,* vol. 113, no. 22, pp. 9978-9985, 2000.

[26] T. L. Hill, An introduction to statistical thermodynamics, 1986.

[27] J. Fester, M. García-Melchor, A. S. Walton, M. Bajdich, Z. Li, L. Lammich, A. Vojvodic and J. V. Lauritsen, "Edge reactivity and water-assisted dissociation on cobalt oxide nanoislands," *Nat. Commun.,* vol. 8, p. 14169, 2017.

[28] L. Xu, Y. Ma, Y. Zhang, B. Chen, Z. Wu, Z. Jiang and W. Huang, "Water Adsorption on a Co(0001) Surface," *J. Phys. Chem. C,* vol. 114, pp. 17023 - 17029, 2010.

[29] M. Kinne, T. Fuhrmann, C. M. Whelan, J. F. Zhu, J. Pantförder, M. Probst, G. Held, R. Denecke and H.-P. Steinrück, "Kinetic parameters of CO adsorbed on Pt(111) studied by in situ high resolution x-ray photoelectron spectroscopy," *J. Chem. Phys.,* vol. 117, no. 23, pp. 10852 - 10859, 2002.

[30] R. B. Moyes and M. W. Roberts, "Interaction of cobalt with oxygen, water vapor, and carbon monoxide: X-Ray and ultraviolet photoemission studies," *J. Catal.,* vol. 49, pp. 216-224, 1977.

[31] C. H. Wu, B. Eren, H. Bluhm and M. B. Salmeron, "An Ambient Pressure X-ray Photoemission Spectroscopy Study of Cobalt Foil Model Catalyst under CO, H2, and their Mixtures," *ACS Catal.,* vol. 7, no. 2, p. 1150, 2017.

[32] G. A. Beitel, A. Laskov, H. Oosterbeek and E. W. Kuipers, "Polarization Modulation Infrared Reflection Absorption Spectroscopy of CO Adsorption on Co(0001) under a High-Pressure Regime," *J. Phys. Chem.,* vol. 100, pp. 12494 - 12502, 1996.

1
2